# Bio-based connections and hybrid planar truss: A parallel genetic algorithm approach for model updating

# Computers and Structures

## Bio-based connections and hybrid planar truss: a parallel genetic algorithm approach for model updating

--Manuscript Draft--

| | |
|---|---|
| **Manuscript Number:** | CAS-D-23-01211R1 |
| **Article Type:** | Research Paper |
| **Keywords:** | Parallel genetic algorithm; connections; High-fidelity FE model; Low fidelity FE model; Hybrid planar truss; Multi-thread parallel analysis |
| **Corresponding Author:** | da shi, Ph.D<br>Zhejiang University<br>Hang zhou, Zhejiang province CHINA |
| **First Author:** | da shi, Ph.D |
| **Order of Authors:** | da shi, Ph.D |
| | Giuseppe Carlo Marano |
| | Cristoforo Demartino |
| **Abstract:** | This paper introduces an innovative 3D plasticity-fracture continuum Finite Element (FE) model that significantly advances the simulation of such truss joints by integrating Hill's yielding criteria with an element removal methodology for fracture simulation. This novel approach captures both plastic and fracture behaviors simultaneously, a capability not sufficiently addressed in existing models. We detail the theoretical framework for these models, including the derivation of constitutive equations and the algorithms necessary for their implementation in ABAQUS. Additionally, it is provided a low-fidelity modeling of truss joints, offering a comprehensive analysis of connector elements, joint models, and parametric modeling via Python scripting. The model's efficacy is demonstrated through identification of connection and of hybrid planar trusses under cyclic loading, which validates the practical applicability of the method. To optimize computational efficiency, we developed a Parallel Genetic Algorithm (PGA) that integrates seamlessly with ABAQUS and Python to facilitate parameter calibration. This integration not only enhances the model's accuracy but also reduces computational load, making it feasible for complex engineering applications. Our findings illustrate a significant improvement in modeling accuracy and efficiency, establishing a robust methodology for analyzing truss joints in bio-based construction materials. |
| **Suggested Reviewers:** | Angelo Aloisio<br>ngelo.aloisio1@univaq.it<br>Angelo Aloisio has long been committed to the study of timber structures |
| | Massimo Fragiacomo<br>massimo.fragiacomo@univaq.it<br>Massimo Fragiacomo has been committed to timber research for a long time |
| | minjuan he, PhD<br>professor, Tongji University<br>hemj@tongji.edu.cn<br>minjuan he has been committed to timber research for a long time |
| | Alex Sixie Cao<br>cao@ibk.baug.ethz.ch<br>Alex Sixie Cao has been committed to timmber research for a long time |
| | Andrea Frangi, PhD<br>Professor, ETH Zurich<br>frangi@ibk.baug.ethz.ch<br>Andrea Frangi has committed to timber resaerch for a long time |
| | yiwei liu, PhD<br>Hunan University<br>295408520@qq.com |

| | |
|---|---|
| | yiwei liu has been committed to material resaerch for a long time |

# Highlights

**Bio-based connections and hybrid planar truss: a parallel genetic algorithm approach for model updating**

Da Shi, Giuseppe Carlo Marano, Cristoforo Demartino

- 3D FE model for bolted steel to timber/glubam connections.
- Merged Hill's criteria with element removal for fractures.
- Integrated ABAQUS and Python for multi-threaded analysis.
- Utilized parallel genetic algorithm (PGA) for efficient calibration of connection models.
- Assessed model on planar trusses under cyclic loading.

# Bio-based connections and hybrid planar truss: a parallel genetic algorithm approach for model updating

Da Shi[a,b,c], Giuseppe Carlo Marano[b], Cristoforo Demartino[c,d,*]

[a] *College of Civil Engineering and Architecture, Zhejiang University, 866 Yuhangtang Road, Hangzhou, 310058 Zhejiang, PR China*

[b] *DISEG, Politecnico di Torino, Dipartimento di Ingegneria Strutturale, Edile e Geotecnica, Corso Duca Degli Abruzzi, 24, Turin, 10128, Italy*

[c] *Zhejiang University - University of Illinois at Urbana Champaign Institute, Zhejiang University, Haining 314400, Zhejiang, PR China*

[d] *Department of Civil and Environmental Engineering, University of Illinois at Urbana-Champaign, Urbana, IL 61801, USA*

**Abstract**

Bolted steel to laminated bio-based material connections experience significant performance challenges due to the nonlinear response and high stress concentrations at their joints. This paper introduces an innovative 3D plasticity-fracture continuum Finite Element (FE) model that significantly advances the simulation of such truss joints by integrating Hill's yielding criteria with an element removal methodology for fracture simulation. This novel approach captures both plastic and fracture behaviors simultaneously, a capability not sufficiently addressed in existing models. We detail the theoretical framework for these models, including the derivation of constitutive equations and the algorithms necessary for their implementation in ABAQUS. Additionally, it is provided a low-fidelity modeling of truss joints, offering a comprehensive analysis of connector elements, joint models, and parametric modeling via Python scripting. The model's efficacy is demonstrated through identification of connection and of hybrid planar trusses under cyclic loading, which validates the practical applicability of the method. To optimize computational efficiency, we developed a Parallel Genetic Algorithm (PGA) that integrates seamlessly with ABAQUS and Python to facilitate parameter calibration. This integration not only enhances the model's accuracy but also reduces computational load, making it feasible for complex engineering applications. Our findings illustrate a significant improvement in modeling accuracy and efficiency, establishing a robust methodology for analyzing truss joints in bio-based construction materials.

*Keywords:* Parallel genetic algorithm, Bio-based connections, High-fidelity FE model, Low fidelity FE model, Hybrid planar truss, Multi-thread parallel analysis

*Corresponding author

*Email addresses:* `da.21@intl.zju.edu.cn` (Da Shi), `giuseppe.marano@polito.it` (Giuseppe Carlo Marano), `cristoforo.demartino@me.com` (Cristoforo Demartino)

## Contents

## 1. Introduction

Structural timber and bamboo are renewable resources that are readily available and possess a significantly lower environmental impact compared to other construction materials of similar strength [1]. The structural performance of timber and bamboo structures is governed by the nonlinear response in the connection zones, where high deformation levels and stress concentrations are developed around the fasteners (nails, dowels or bolts) [2, 3, 4]. These critical zones are particularly vulnerable to significant load reversals over the structure's lifespan, notably under extreme conditions like earthquakes or severe winds [5]. Given these factors, it is crucial to thoroughly investigate the nonlinear behaviors of timber and bamboo connections, especially from the onset of large deformations to the point of failure [6]. Compared to traditional materials such as concrete and steel, bio-based construction materials like timber and bamboo are more susceptible to fracturing [2]. Despite this vulnerability, few existing models for bio-based connections effectively incorporate the critical fracture modes while simultaneously accounting for plastic behavior. This gap highlights the need for advanced modeling techniques that can accurately simulate both the plastic and fracture behaviors of bio-based materials, ensuring a more comprehensive understanding and robust design of these eco-friendly construction options.

Finite Element (FE) modeling of timber or bamboo joints is pivotal in understanding the mechanical behavior and ensuring the structural integrity of timber constructions [7, 8]. Two primary approaches are adopted for this purpose: $(i)$ explicit component modeling and $(ii)$ representative element modeling. Explicit component modeling involves detailed modeling of each joint element, such as timber and connectors like steel dowels, which enables precise simulation of their interactions and mechanical performance. This method, though computationally intensive, provides a granular insight into the behavior of the joints, especially under varying mechanical stresses [e.g., 9, 10]. Alternatively, the representative element approach simplifies the joint modeling by encapsulating it into a single element with predefined mechanical properties, which reduces computational demands and facilitates easier integration into structural-level analyses [11]. This method requires the programming of user-subroutines, allowing the joint model to be applied to either member- or structural-level analyses [12, 13]. However, the complexity of this programming often leads to convergence issues. Consequently, there is a scarcity of FE modeling approaches that are both simple to implement and versatile enough to be integrated into various commercial FE packages for structural-level analysis. This limitation underscores the need for more user-friendly and robust modeling solutions in the field.

Using the second approach, the representative element model, a significant challenge arises in the calibration of parameters that define the hysteretic model. Accurate parameter calibration is crucial for ensuring that the model reflects true mechanical behaviors, especially under cyclic loading conditions typical in seismic analysis. The calibration process involves determining the appropriate parameters defining the stiffness, strength, and damping properties that can predict the hysteretic behavior accurately. The complexity of calibrating these parameters often requires sophisticated optimization algorithms and can be a source of significant computational overhead, further complicating the use of FE models in practical engineering applications.

Genetic algorithms are highly suited for a broad range of problems in structural engineering, particularly for optimization and damage identification tasks [14]. However, they often require extensive computation time, which can be a disadvantage [15]. The evaluation of the fitness function typically represents the most time-consuming step within these algorithms [16, 17]. Parallel Genetic Algorithms (PGAs) represent an evolution of traditional genetic algorithms (GAs) that harness parallel computing environments to enhance efficiency and scalability [18]. An effective solution to mitigate this issue involves leveraging high-performance computing techniques, such as distributed or parallel computing [19]. Parallel execution significantly reduces the time required for genetic operations and fitness evaluations. In a master-slave configuration, the workload is distributed among multiple processors. While numerous slave threads handle multitasked loops, a single master thread is dedicated to managing the sequential aspects of the algorithm and ensuring coordination, communication, and synchronization across the network. This parallel computing feature is particularly advantageous for metaheuristic search techniques, enabling simultaneous processing by multiple processors without the need for inter-processor communication [20].

In the evolving field of structural engineering, novel optimization algorithms play a critical role in enhancing the accuracy and efficiency of structural analysis and damage identification. Recent studies demonstrate significant advancements in this domain through the development and application of innovative metaheuristic algorithms. For instance, the introduction of the BCMO-ANN algorithm has markedly improved the vibration and buckling optimization of functionally graded porous microplates [21]. Similarly, the Shrimp and Goby association search algorithm has been effectively applied to damage identification in large-scale and complex structures [22]. Optimization of artificial neural networks architecture also continues to enhance predictive capabilities in geotechnical engineering [23]. Additionally, innovative strategies like the variable velocity strategy particle swarm optimization (VVS-PSO) have shown promise in structural damage assessment [24]. Finally, efficient stochastic-based models have been developed for more precise damage identification in plate structures [25]. Collectively, these advancements underscore a significant shift towards more robust and precise methodologies in structural engineering analysis.

In this context, this paper advances structural engineering by addressing critical gaps in modeling bio-based connection systems, specifically those involving bolted steel to Laminated Veneer Lumber (LVL) and glued laminated bamboo (glubam). Existing models inadequately capture the orthotropic nature of these materials and their susceptibility to cracking under stress [26, 27]. The proposed 3D continuum FE model, developed in ABAQUS, incorporates the Hill yield criterion for accurate orthotropic properties and an element removal criterion via UMAT to simulate cracking behaviors. We introduce a simplified hybrid truss model that merges advanced joint modeling techniques with traditional wire elements, enhancing the reliability of bio-based connection systems. A novel aspect of our approach is the FE model updating framework that uses multi-threaded parallel analysis with genetic algorithms, optimizing computational efficiency and model accuracy. To manage the complex parameter space, we utilize PGA, implemented in Python, to minimize discrepancies between predicted and actual force-time histories, crucial for improving predictive accuracy. Our approach introduces practical, simplified modeling techniques by combining multi-axial connector and spring elements, accommodating various behaviors like elasticity and plasticity, and effectively capturing joint force-deformation characteristics. This study presents a comprehensive FE model updating framework, significantly enhancing the robustness and accuracy of structural models for engineers optimizing complex analyses in real-world applications.

After this introduction, the paper is organized six main sections. Section 2 delves into the formulation of plasticity-fracture continuum FE models for bio-based connections, detailing the connection configuration, mechanical problems, and material behaviors. Section 2.6 explores the axial behavior modeling of LVL and glubam connections, including FE implementation and results validation. Section 2.6 explores the high-fidelity axial behavior modeling of LVL and Glubam connections, including FE implementation and results validation. Section 3 focuses on the low-fidelity modeling of truss joints, offering a comprehensive analysis of connector elements, joint models, and parametric modeling via Python scripting. Section 4 addresses model identification based on high-fidelity model outputs, utilizing parallel genetic algorithms and parallel computing systems for multi-thread parameter identification and model updating. Section 5 provides details on the model updating of hybrid planar trusses. Finally, Section 6 presents the conclusions drawn from the study, summarizing key findings and their implications.

## 2. Formulation of plasticity-fracture continuum FE model for bio-based connections

### *2.1. Connection configuration and mechanical problem*

Bolted connections with slotted in steel plate are considered in this study. These connections are composed of beam (LVL or Glubam), Grade 8.8 high strength bolts and Q235 steel plate. Holes are drilled on the LVL and Glubam components and steel plates. Bolts protruding from these holes are adopted to connect the steel plate with LVL and glubam components. All the joints were designed following geometric requirements of GB50005 [28]. Four different configurations of connections accounting for different test variables including materials (Laminated Veneer Lumber (LVL) and Glued Laminated Bamboo (glubam)), bolt diameter (8 mm or 10 mm) were considered. Details regarding the joints geometry and configurations are presented in Figure 1.

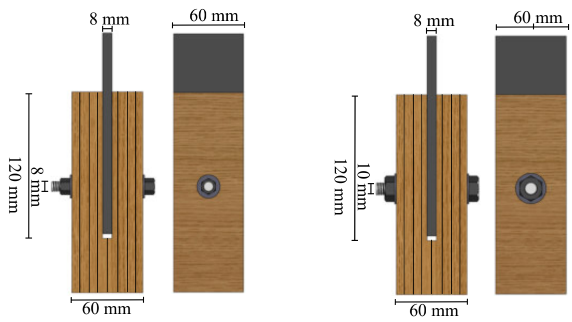


(a) 8mm bolt (b) 10mm bolt

Figure 1: Configuration of connections accounting for different variables. Adapted from Shi et al. [29].

LVL and glubam are typical bio-based laminated materials, which are treated as orthotropic materials. As shown in Figure 2, the material orientation can be divided into laminated direction, grain direction and perpendicular to grain direction and they show different mechanical properties in different orientations. Under axial loading, this type of connections tend to exhibit two typical damage pattern, namely (1) crushing deformation around bolt and (2) block shearing-out above the bolt as shown in Figure 3.

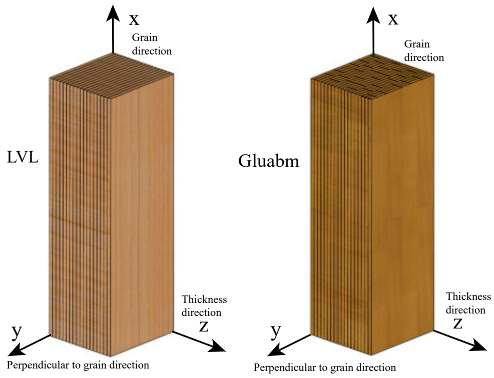


Figure 2: Materials orientation and coordinate system of LVL and glubam.

Bio-based construction materials are prone to delamination inducing fracture, while to date, few models for bio-based connections is able to incorporate its most important fracture mode while considering plastic behavior simultaneously. To carry out a more robust performance-based assessment toward laminated timber and bamboo structures, formulating a high-fidelity FE model capable of characterizing plasticity and fracture behavior of orthotropic materials simultaneously is necessary. Integrating plastic behavior and cracking behavior into one constitutive law is a tough problem that need to be solved in the modelling framework for bio-based connections.

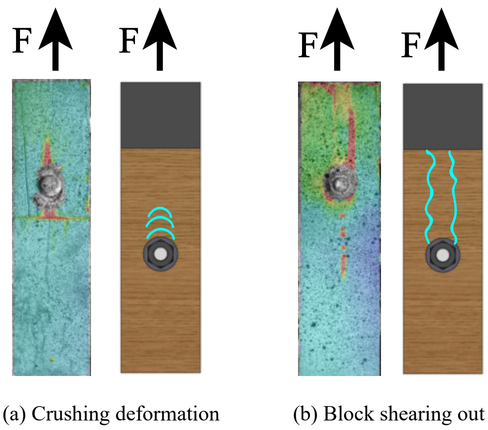


Figure 3: Typical damage pattern of bio-based connections under axial loading.

### *2.2. Orthotropic linear-elastic behavior of LVL and glubam*

Before the initiation of yielding (compression) or failure (tension and shear), the strain-stress relationship for Laminated Veneer Lumber (LVL) and glued laminated bamboo (glubam) can be precisely described using a linear-elastic orthotropic compliance tensor. This relationship is defined by:

$$\varepsilon = C^e : \sigma \tag{1}$$

where $C^e$ is the fourth-order orthotropic liner-elastic compliance tensor. The matrix form of $C^e$ and corresponding stiffness tensor $D^e$ are listed in Appendix A.

In this constitutive model, the orthotropic axes—labeled as 1, 2, and 3—align with the grain direction (X-axis), perpendicular to the grain direction (Y-axis), and the laminated direction (Z-axis), respectively, as illustrated in Figure 2. The anisotropic nature of LVL and glubam results in distinct values for the elastic moduli, shear moduli, and Poisson's ratios along these three orthogonal axes. However, due to the symmetry property of $C^e$ and $D^e$, the following conditions hold:

$$\frac{\mu_{12}}{E_1} = \frac{\mu_{21}}{E_2}; \frac{\mu_{23}}{E_2} = \frac{\mu_{32}}{E_3}; \frac{\mu_{13}}{E_1} = \frac{\mu_{31}}{E_3} \tag{2}$$

To comprehensively describe the linear-elastic orthotropic behavior of these materials, it is essential to determine a total of nine mechanical parameters: three elastic moduli ($E_1$, $E_2$, $E_3$), three shear moduli ($G_{12}$, $G_{13}$, $G_{23}$) and three Poisson's ratios ($\mu_{1,2}$, $\mu_{1,3}$, $\mu_{2,3}$).

### *2.3. Orthotropic plastic behavior of LVL and glubam*

Hill's yielding criterion is widely used to characterize plastic behavior of orthotropic materials [30, 31, 32, 33], which takes into considerations material and yielding orthotropy [34]. Hill's yielding criteria has been successfully applied in other researches such as CLT dowel-type connections [35], timber joints with glued-in rods [36] and traditional timber mortise-tenon joints [37].

In this study, we derive the elastoplastic stiffness of orthotropic materials initially in tensor form based on Hill's yield criterion. Subsequently, we present the matrix form of the corresponding elastoplastic stiffness, detailed further in Appendix B. This structured approach allows for a comprehensive analysis and a better understanding of the mechanical behavior under various loading conditions, enhancing the predictive capabilities of our models for bio-based construction materials.

#### *2.3.1. Tensor form of constitutive law for Hill's yield criterion in orthotropic material*

For orthotropic material, Hill's yield criterion is defined as follows:

$$f(\sigma_{ii}) = \overline{\sigma} = \sqrt{\frac{1}{2}\left[\alpha_{12}(\sigma_{11}-\sigma_{22})^2 + \alpha_{23}(\sigma_{22}-\sigma_{33})^2 + \alpha_{31}(\sigma_{33}-\sigma_{11})^2\right] + 3\alpha_{44}\sigma_{12}^2 + 3\alpha_{55}\sigma_{23}^2 + 3\alpha_{66}\sigma_{31}^2} \tag{3}$$

where $f$ is the yielding function; $\overline{\sigma}$ is the equivalent stress; $\sigma_{11}$, $\sigma_{22}$ and $\sigma_{33}$ are the normal stresses; $\sigma_{12}$, $\sigma_{23}$ and $\sigma_{31}$ are the shear stresses; $\alpha_{ii}$ are anisotropic parameters.

In practice, changes in strain (deformation) are tracked incrementally. The total strain increment, $d\varepsilon_{ij}$, is considered as the sum of elastic (reversible) strain, $d\varepsilon^e_{ij}$, and plastic (permanent) strain, $d\varepsilon^p_{ij}$:

$$d\varepsilon_{ij} = d\varepsilon^e_{ij} + d\varepsilon^p_{ij} \tag{4}$$

The plastic component of the strain is determined using the flow rule, which relates it to the yield function:

$$d\varepsilon^p_{ij} = \lambda \frac{\partial f}{\partial \sigma_{ij}} \tag{5}$$

where $\lambda$ is a factor that can be assumed that $\lambda = hdf$ where $h$ is the hardening modulus. Then,

$$d\varepsilon_{ij} = d\varepsilon^e_{ij} + hdf \frac{\partial f}{\partial \sigma_{ij}} \tag{6}$$

The stress-strain relationship in elastic stage can be assumed as:

$$\sigma_{kl} = a^e_{klij} \varepsilon^e_{ij} \tag{7}$$

where $a^e_{klij}$ is the elastic stiffness tensor.

From Eq. 6, it can be obtained that:

$$a^e_{klij} d\varepsilon_{ij} = d\sigma_{kl} + hdf a^e_{klij} \frac{\partial f}{\partial \sigma_{ij}} \tag{8}$$

and

$$\frac{\partial f}{\partial \sigma_{kl}} a^e_{klij} d\varepsilon_{ij} = \frac{\partial f}{\partial \sigma_{kl}} d\sigma_{kl} + hdf \frac{\partial f}{\partial \sigma_{kl}} a^e_{klij} \frac{\partial f}{\partial \sigma_{ij}} \tag{9}$$

It is worth noting that:

$$df = \frac{\partial f}{\partial \sigma_{kl}} d\sigma_{kl} \tag{10}$$

Substituting Eq. 10 into Eq. 9:

$$hdf = \frac{\frac{\partial f}{\partial \sigma_{kl}} a^e_{klij} d\varepsilon_{ij}}{\frac{1}{h} + \frac{\partial f}{\partial \sigma_{pq}} a^e_{pqrs} \frac{\partial f}{\partial \sigma_{rs}}} \tag{11}$$

Substituting Eq. 11 into Eq. 8:

$$d\sigma_{kl} = \left( a^e_{klij} - \frac{a^e_{klfg} \frac{\partial f}{\partial \sigma_{fg}} \frac{\partial f}{\partial \sigma_{mn}} a^e_{mnij}}{\frac{1}{h} + \frac{\partial f}{\partial \sigma_{pq}} a^e_{pqrs} \frac{\partial f}{\partial \sigma_{rs}}} \right) d\varepsilon_{ij} \tag{12}$$

The above equation is the tensor form of the constitutive equation for orthotropic material, and where the part shown in bracket of the above equation:

$$a_{klij} = a^e_{klij} - \frac{a^e_{klfg} \frac{\partial f}{\partial \sigma_{fg}} \frac{\partial f}{\partial \sigma_{mn}} a^e_{mnij}}{\frac{1}{h} + \frac{\partial f}{\partial \sigma_{pq}} a^e_{pqrs} \frac{\partial f}{\partial \sigma_{rs}}} \tag{13}$$

is the elasto-plastic stiffness tensor. The hardening modulus in the above equations is defined as follows:

For hardening materials, plastic work is defined as:

$$dW_p = \sigma_{ij} d\varepsilon^p_{ij} \tag{14}$$

Substituting Eq. 5 and Eq. 3 into Eq. 14:

$$dW_p = \lambda \bar{\sigma} \tag{15}$$

On the other hand, plastic work can also be represented by equivalent stress and equivalent plastic strain:

$$dW_p = \overline{\sigma} d\overline{\varepsilon}_p \tag{16}$$

Combining above Eqs. 15 and 16:

$$\lambda = d\overline{\varepsilon}_p = \frac{d\overline{\sigma}}{\overline{H}} \tag{17}$$

where $\overline{H}$ is the slope of $\overline{\sigma} - \overline{\varepsilon}_p$ curve and can be determined from experimental tests. Notice that:

$$\lambda = hdf = hd\overline{\sigma} = \frac{d\overline{\sigma}}{\overline{H}} \tag{18}$$

Therefore:

$$h = \frac{1}{\overline{H}} \tag{19}$$

In practical calculations, the relationship between the equivalent stress $\overline{\sigma}$ and the equivalent strain $\overline{\varepsilon}$ is often derived from empirical material test results in a principal material direction. Differences in material properties across other directions are systematically accounted for by utilizing anisotropic parameters, denoted as $\alpha_{i,j}$. The procedure for the determination of anisotropic parameters $\alpha_{ij}$ is discussed in Appendix C.

### 2.4. Fracture behavior

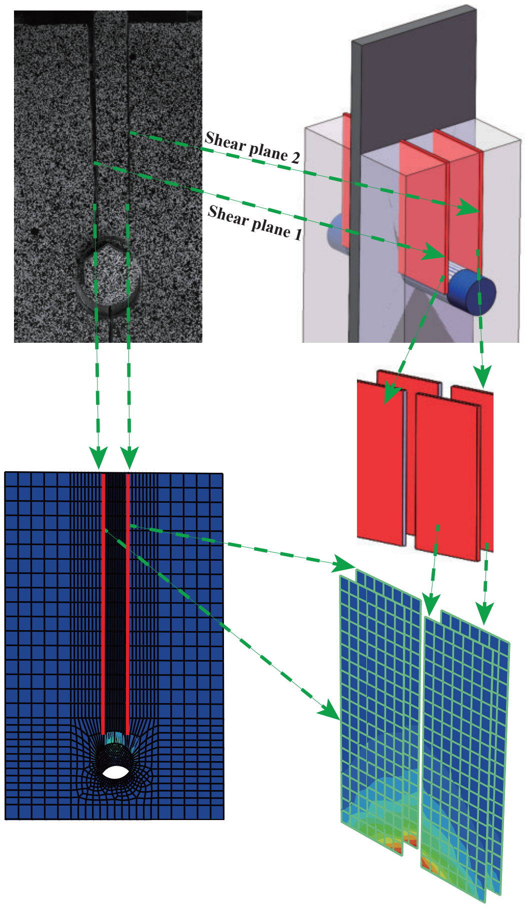


Figure 4: Potential shear cracking zone.

Although the softening behavior of LVL and glubam was simulated to some extent by Hill's yield criterion, no crack propagation was considered in this criterion. Herein, an attempt was made to simulate the cracking behavior by removing the damaged elements along the potential cracking zone [38, 39, 40] as shown in Figure 4. The fracture of LVL and glubam, majorly manifested in shearing-out form, was the key factor leading to the failure of the connection [41, 42]. To model this behavior, a user subroutine, UMAT was integrated in ABAQUS to implement the damage function [42, 43] defined as:

$$D = \left(\frac{\overline{\sigma}}{f_{t,90}}\right)^2 + \left(\frac{\overline{\tau}}{f_{v,0}}\right)^2 \tag{20}$$

where $\overline{\sigma}$ and $\overline{\tau}$ are the perpendicular-to-grain tensile stress ($\sigma_{22}$) and parallel-to-grain shear stress ($\sigma_{12}$) respectively, and $f_{t,90}$ and $f_{v,0}$ are the perpendicular-to-grain tensile strength and parallel-to-grain shear strength respectively, which can refer to Shi et al. [44].

The damage variable $D$ in Eq. 20 was utilized in the subroutine such that when its value reaches one, the subroutine passes the zero stress state to the element, and the element was deleted from the mesh. The size of the removed elements is about 0.1 mm wide and to guarantee convergence. The total length of element-removing area was extended from the wall of bolt hole to the upper end of the member and its area was equal to the area of two shear failure plane as shown in the red areas in Figure 4. When the block between two shear plane was totally sheared out, the calculation terminates.

The procedure for the element removal is:

1. Obtain perpendicular-to-grain tensile stress $\sigma_{22}$ and parallel-to-grain shear stress $\sigma_{12}$ from state variable in ABAQUS subroutine and check damage variable $D$.

$$D_e = \left(\frac{\sigma_{22,e}}{f_{t,90}}\right)^2 + \left(\frac{\sigma_{12,e}}{f_{v,0}}\right)^2 = 1 \tag{21}$$

   where $e$ is an element number, which links to the elements to be checked.

2. An element is removed if it satisfies the condition in Eq. 21 by setting its material properties to zero. When the $ii$-th is removed, there will be a redundancy in the Jacobian matrix which will affect the tangential stiffness matrix $\boldsymbol{K}_T$:

$$\boldsymbol{K}_T = \begin{bmatrix} K_{11}^e & \cdot & \cdot & \cdot & K_{1i}^e & \cdot & \cdot & \cdot & K_{1n}^e \\ & \cdot & & & \cdot & & & & \\ & & & \cdot & \cdot & & & & \\ K_{i1}^e & \cdot & \cdot & \cdot & K_{ii}^e = 0 & & & & K_{in}^e \\ & & & & \cdot & \cdot & & & \\ & & & & \cdot & & & \cdot & \\ K_{n1}^e & \cdot & \cdot & \cdot & K_{ni}^e & \cdot & \cdot & \cdot & K_{nn}^e \end{bmatrix} \tag{22}$$

   where $n$ is the total number of elements.

3. Start a new step based on a redundant structural tangential stiffness (i.e., remove the $ii$-th element associated rows and columns) and repeat steps 1 and 2.

### *2.4.1. Algorithm design for Plasticity-Fracture behavior*

The algorithm of the plasticity-fracture constitutive for LVL and glubam is shown in Table D.7 in Appendix D. First the material parameters were input including materials constants, reference yielding stress, anisotropic parameters and hardening function and hardening modulus.Then the orthotropic elastic matrix was formed and the total elastic stress tensor is calculated. In the next step the equivalent stress is evaluated into the yield function in order to determine if there is plasticity or not. In case of plasticity, the plastic strain increment is calculated according to hardening modulus and plastic flow rule. Then stress components is obtained to evaluate the damage function. The damage status can be reflected by a State

Variable in ABAQUS subroutine. In case of damage, the value of State Variable equal to 0 and the element is deleted from the mesh. In case of no damage, the value of State Variable keeps 1 and the stress component is still renewed according to normal elasto-plastic stiffness matrix. Then the next iteration starts and the calculation will be terminated until all elements on the target crack plane were removed or divergence occurs.

### *2.4.2. Experimental validation of plasticity-fracture constitutive law*

Figure 5 compares the experimental and simulated results in one representative embedment test by using the constitutive model as described above. The material constitutive law of LVL is programmed in the subroutine according to Table D.7, where both the element removal criterion and Hill's yielding criterion are considered. The simulated cracking path is in good agreement with the real cracking path observed from test. Moreover, a progressive descending stage can be observed in the simulated loading-embedment displacement curves (more details related to this model could be found in Shi et al. [44]), which corresponding to continuously removed elements.

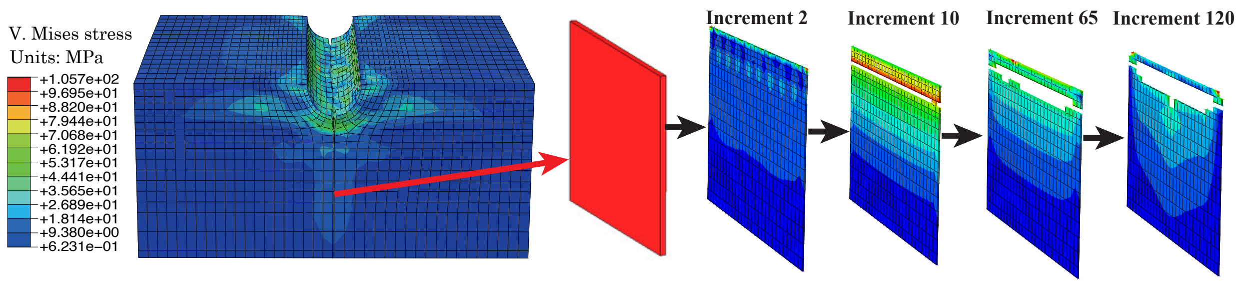


Figure 5: Evolution of element status in the pre-determined crack plane as fracture propagates in FE model of embedment test.

## *2.5. Effective foundation model properties for embedment zone*

In this study, for timber and bamboo elements in the embedment zone (the area around the bolt, see yellow area in Figure 7), wood foundation model was used to describe the local crushing behavior due to embedment compression. In wood foundation model, material hardening was considered by bilinear fitting the performance curves obtained from the embedment compression tests (see our previous study [44] ) as shown in Figure 6. The relative LVL and glubam constitutive in the embedment zone are then determined by the fitting result from the embedment compression tests according to the analysis method proposed by Hong and Barrett [45]. The foundation modulus and foundation yield point are defined based on the load-embedment displacement curve from embedment compression tests. In the fitted bilinear curve, an initial slope and a break point between two linear regions were identified. The nominal foundation modulus and the nominal yield point can then be calculated as:

$$k = \frac{P_y}{W_y} \tag{23}$$

where $k$ is nominal foundation modulus (MPa), $P_y$ is the yield load in the bilinear load/unit length-embedment displacement curve (N/mm), and $W_y$ is the yield deformation in the load/unit length-embedment displacement curve (mm).

In the wood foundation model, the nominal foundation modulus along parallel-to-grain directions ($E_{1,F}$) were determined according to experimental results as discussed above, while the effective foundation modulus Hong and Barrett [45] along other directions ($E_{2,F}$, $E_{3,F}$, etc.) were derived by proportional transformation using the same ratio of $E_1$ and $E_{1,F}$ as following:

$$\frac{E_{1,F}}{E_1} = \frac{E_{2,F}}{E_2} = \frac{E_{3,F}}{E_3} \tag{24}$$

The Poisson's ratios in the wood foundation model ($\mu_{12,F}$, $\mu_{13,F}$, etc.) were the same as the normal materials property. The final parameters for the wood foundation model could be found in our previous research [44]. The elastic constants in the three orthotropic directions were reduced significantly in the wood foundation model compared to the elastic constants directly obtained from the normal materials test. This was consistent with the approach proposed by Hong and Barrett [45] who adopted effective (reduced) foundation properties (i.e., properties of the material around the bolt) to match the observed stiffness.

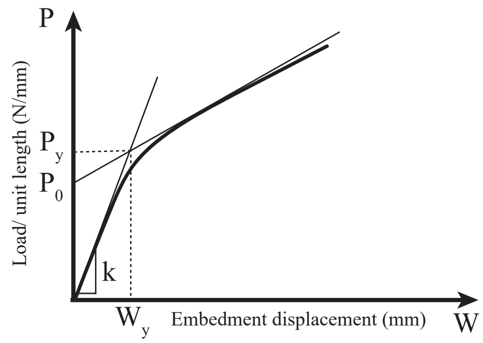


Figure 6: Bilinear backbone curve fitted to bolt-embedment data.

### 2.6. *High-fidelity axial behavior modelling*

#### 2.6.1. *FE implementation*

Figure 9 shows the finite element model for bolted connection developed in ABAQUS. The 3D FE model (FEM) consists of one steel plate, bolts and main members (LVL or glubam). The geometry of the connection components are the same as the geometry of the tested specimens [44].

All the components were modeled with eight-node brick elements (C3D8) in the ABAQUS software. The bolt and steel plate was modeled as isotropic elastic-perfectly plasticity. For the bolts and steel plate, the module of elasticity (MOE) is 210 GPa and the Poisson ratio is 0.3 based on C10B21 steel properties. The yield stress is 345 MPa for steel plate. The yield stress is 721.52 and 823.98 MPa for $\Phi 8$ and $\Phi 10$ bolts, respectively.

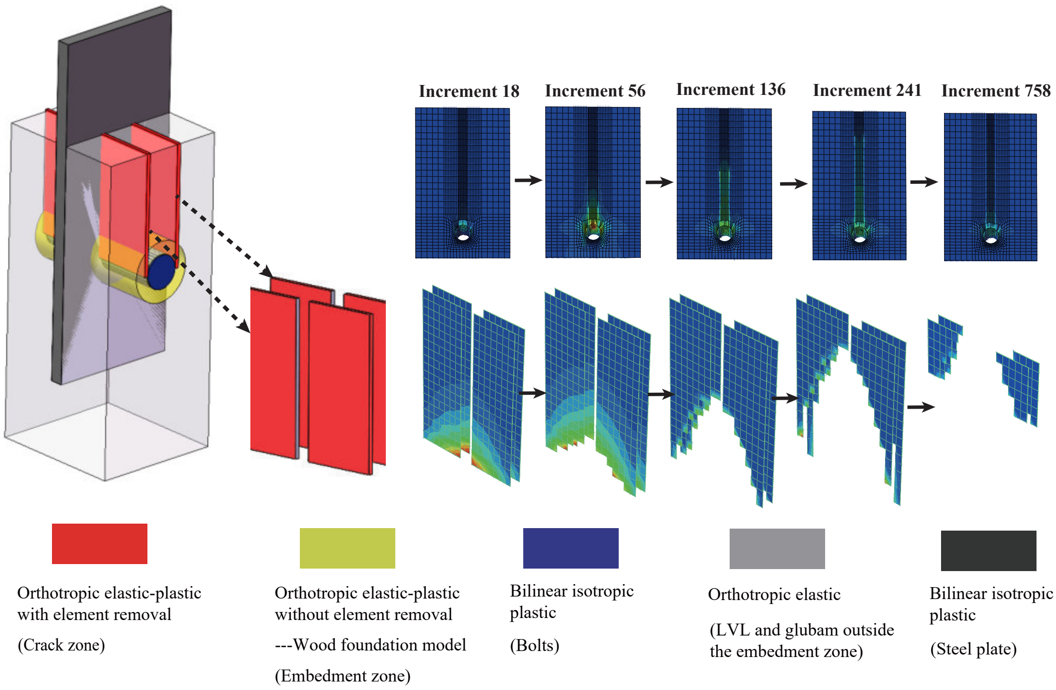


Figure 7: Material constitutive partitioning of the numerical model and evolution of element status in the pre-determined crack plane as fracture propagates in FE model (G-M-S10) of connection test. Adapated from Shi et al. [44].

It has been proved from previous studies [45, 37, 46, 47] that the constitutive of the elements outside the embedment zone (gray area in Figure 7) was negligible while that in the embedment zone (see red area in Figure 7) was dominating the response. Therefore, the LVL or glubam block was modeled with different material properties for elements inside and outside the embedment zone, and crack zone. The material partitioning of the block is shown in Figure 7. The elements outside the embedment zone (gray area in Figure 7) were assumed to be orthotropic linear elastic elements, and the Young's modulus was determined by compression tests of prism specimen (refer to Shi et al. [44]). An adaptive mesh was adopted with mean mesh-size equal to around to 3 mm. In the embedment zone, orthotropic elastic-plastic constitutive (Hill's yielding criteria) was used and the Hill's yielding criteria were implemented by directly inputting the parameter of Hill's yielding function in the ABAQUS user interface without establishing subroutine. The material properties in the embedment zone were equal to the effective foundation model properties (Section

2.5). As for elements in crack zone (red area in Figure 7), orthotropic elasto-plastic constitutive (Hill's yielding criteria) with progressive element removal was implemented. In the crack zone, the Hill's yielding criteria and element removal were both implemented by establishing subroutine. The thickness in the crack zone was set equal to 0.1mm and the mesh-size equal to around to 3 mm. The material parameters of the glubam and LVL referred to the experimental results in Shi et al. [44].

The interface property of all the contact surfaces is set as hard contact. The Coulomb friction coefficient of all contact surfaces is taken as 0.5. Moreover, to model the initial slip stage caused by the hole clearance between the bolt and hole wall of timber elements [48], 0.5 mm tolerance between the interface of bolt and timber elements in ABAQUS model is set.

### 2.6.2. FEM results and experimental validation

The experimental and numerical results of the bolted to steel bio-based connection subjected to tension monotonic loading and cyclic loadingwere compared. The detailed test setup and instrument for truss joints is shown in Figure E.24.

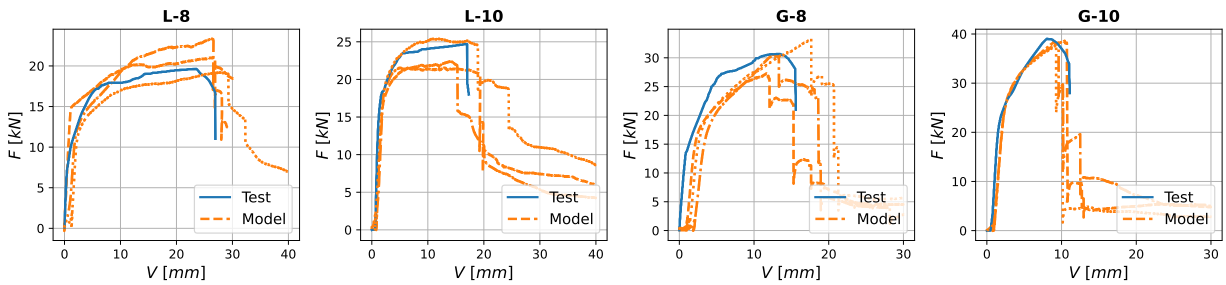


Figure 8: Load (F) vs. displacement (V) results of FEM analyses compared to experimental results under monotonic loading for specimens L-8, L-10, G-8, G-10.

The simulation results of the failure modes for a typical specimen obtained by the FEM are shown in Figure 9, where a typical shearing-out failure mode can be observed. A comparison of element status in the predetermined crack plane as fracture propagates is shown in Figure 7, where the vanishing elements on the fracture plane gradually formed the final fracture path.

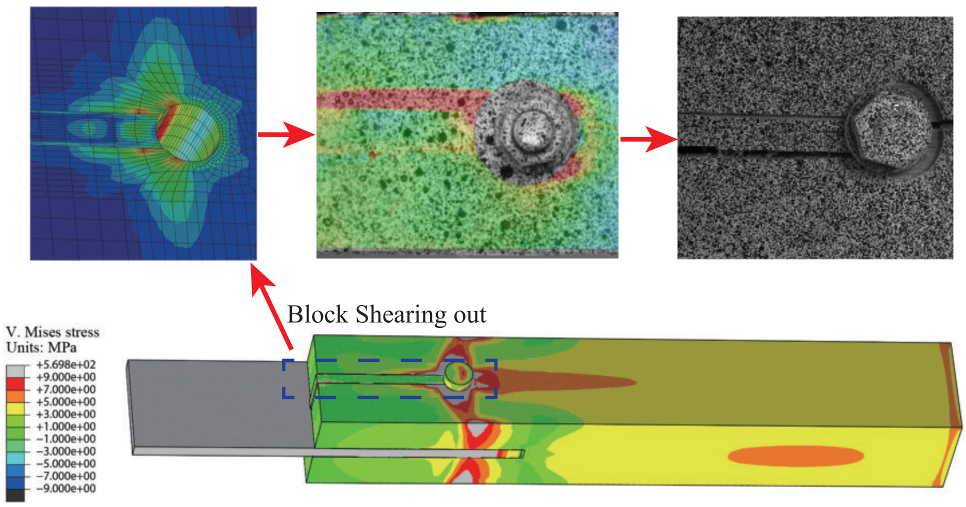


Figure 9: Comparison between simulated failure modes and tested failure modes. Adapated from Shi et al. [44].

From Figure 8, it can be noticed the proposed plasticity-fracture model is able to reproduce the stiffness degradation shown by the monotonic experimental curves, eventually reaching a maximum load plateau and then failure. Moreover, the prediction of the maximum load and the ultimate deformation is good. Figure 10 compares the experimental and numerical results for specimens L-8 under cyclic loading. It can be observed the proposed plasticity-fracture model is able to reproduce the envelop curve, pinching effect, stiffness degradation and strength degradation shown by the experimental curves. In general, the overall nonlinear monotonic and hysteretic response of the bolted to steel bio-based connection is accurately predicted by the new plasticity-fracture continuum FE model proposed in this study.

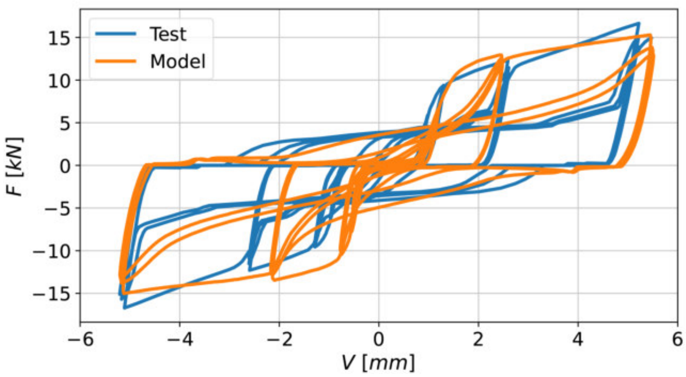


Figure 10: Load (F in kN) vs. displacement (V in mm) results of FEM analyses compared to experimental results under cyclic loading for Specimen L-8.

To quantitatively compare the FEM prediction capabilities , the FE-predicted responses are compared with the true responses using the Relative Root Mean Square Errors (RRMSE). The RRMSE provides a measurement of the error between two signals, $\mathbf{a}$ (tested value) and $\mathbf{b}$ (predicted value), and is defined as

$$RRMSE\left(\mathbf{a},\mathbf{b}\right)=\frac{\sqrt{\left[\frac{1}{N_s}\sum_{i=1}^{N_s}\left(a_i-b_i\right)^2\right]}}{\sqrt{\left[\frac{1}{N_s}\sum_{i=1}^{N_s}\left(a_i\right)^2\right]}}\times 100\,(\%) \tag{25}$$

where $N_s$ denotes the total number of data samples in the signals.

Table 1 presents the $RRMSE$ (see Eq. 25) computed between the actual (tested) responses and those predicted by FE model. In terms of monotonic responses, the $RRMSE$ remain below 15% and in terms of hysteresis responses, the $RRMSE$ remain below 20%, which confirmed the validity of the FE model proposed in this study.

Table 1: $RRMSE$ (see Eq. 25) between the true observed responses and the corresponding initial and FE-predicted responses.

| Monotonic responses | | | | Hysteresis response |
|---|---|---|---|---|
| L-8 | L-10 | G-8 | G-10 | L-8 |
| 11.56% | 8.56% | 14.68% | 7.62% | 19.35% |

## 3. Low-fidelity model for joints

To achieve a balance between model prediction accuracy and computational burden, a simplified and versatile phenomenological model that specify the envelope path and associated hysteresis is proposed in this study. The simplified modelling method used in this study is inspired by the methodology provided in Xu et al. [9] which involves combining a series of connector elements from which the hysteresis behaviour of the joints is generated. The methodology is convenient to apply to timber truss structures, and the method is advanced herein. More specifically, the truss joint is modelled by a series of two-dimensional axial connector elements which are available in ABAQUS as CONN2D2. Basic behaviours are assigned to each element, namely, elasto-plastic behaviour (herein EP elements), STOP behaviour (herein S elements) and LOCK behaviour (herein L elements). In the present joint model, the positions of all nodes locate at the same position and mechanical behaviours are assigned to the tension and compression degree of freedom (DOF) of the connector elements only. Therefore, the plot of the FE mesh is a series of nodes positioned at the same location. In order to provide a more intuitive illustration, the tension and compression DOF of the elements are transformed to one dimensional translation. The connector elements are illustrated in Figure 11 while the joint model is shown schematically in Figure 12.

### 3.1. Behavior of connector elements

In the model reported herein, elasto-plastic elements with one DOF are utilised as only uniaxial behaviour needs to be considered. As a result, there are four parameters that need to be defined for the EP element, namely ($i$) elastic stiffness, ($ii$) yield strength, ($iii$) post-yield stiffness, and ($iv$) hardening rule.

The hardening rules used within this study includes isotropic hardening and kinematic hardening. The rules are respectively shown in Figure 11 (d) and (e). The isotropic hardening rule specifies that the centre of the yield surface remains at its original position and that the yield surface expands with positive post-yield stiffness. The kinematic hardening rule specifies that the shape of the yield surface remains the same and that the centre of the yield surface moves with the yield stress.

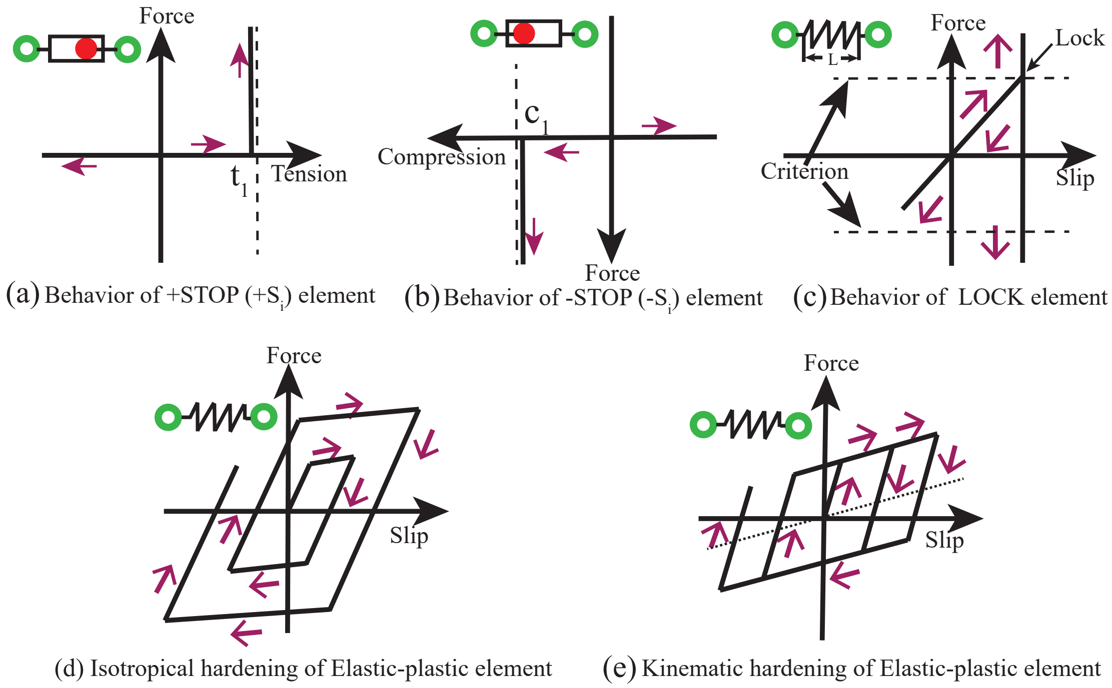


Figure 11: Behavior of connector elements.

The behaviour of the S elements can be described as a slider positioned in a slot that has a finite length. This type of element contains two nodes (i.e., one node is the slider, and the second node is the slot) as provided in Figure 11 a and b. The minimum and maximum deformation is limited by the two boundaries of the slot node, while deformation of the element occurs without friction within the limit of the two boundaries.

The behaviour of an L element is shown in Figure 11 c. The element is assigned a threshold value which is expressed in terms of either deformation or internal force. Before the threshold value is achieved though, the element behaves according to the original properties that are assigned to it. The element will be “locked ”and defined as a rigid body when it achieves the threshold value. In this case, the distance between the two nodes will no longer change. Finally, the L element is defined by linear-elastic behaviour with internal force as the threshold criterion.

### 3.2. Proposed joint model

The physical mechanisms contributing to the pinched-style hysteresis behaviour of the bolt-type timber joints are comprised of three basic stages.

1. LOADING: The bolts are in contact with the timber hole (i.e., a hole that accommodates a steel bolt), the timber is subjected to bearing load and the bolts are subjected to bending. In this stage, the bolts and timber work together to resist the external load;
2. UNLOADING: The bolts separated from the bearing wall of the hole and slide in the deformed hole. In this stage, friction force is the dominant action resisting the applied load;
3. RELOADING/REVERSE LOADING: The bolts are bent in an opposing manner and slide in the deformed hole until they fully contact with the wall of the hole.

Based on these physical interpretations, a model is proposed in this paper that is informed from three key assumptions: (1) EP elements are used in conjunction with slot elements in order to represent the bearing of timber as well as the permanent deformation of the hole; (2) friction force and reverse bending of the bolts are all considered in the steel bolt model; (3) three groups of EP + S elements are connected in parallel in order to achieve yield of the timber representing contact between the bolts and timber hole in the reloading/reverse loading stage. Details of the model formulation are now further elaborated upon.

As indicated at the beginning of this section, the contributions of the steel bolt, timber bearing and strengthening schemes are modelled individually while the overall behaviour of the joint involves the superposition of the actions contributed by all components. Figure 12 provides key details about the joint model. The overall model is shown schematically in Figure 12 a. In addition, the combinations of connectors shown in Figure 12 b and d represents the behaviour of the steel bolt action and timber bearing action, respectively, while their monotonic force-slip behaviours are plotted schematically in Figure 12 (c) and (e), respectively. According to the assumptions of superposition, the capacity of the joint is given by:

$$F\left(V\right) = F_s\left(V\right) + F_b\left(V\right) \tag{26}$$

where $F$ is the joint force, $F_s$ is the force contributed by the steel bolt model, $F_b$ is the force contributed by the timber bearing model, and $V$ is the slip of the joint. Details of these three models are provided in the following sections.

#### 3.2.1. Bolt model

The behaviour of the steel bolt is modelled by connecting an EP element, an L element and a S element in series (see Figure 12 b). The L criterion is set to be equal to the yield strength of the $EP_s$ element. The elastic stiffness obtained by the steel bolt model can therefore vary before and after yielding of the bolt, thus simulating the embedding process of the bolts with a lower initial stiffness before yielding. The S elements

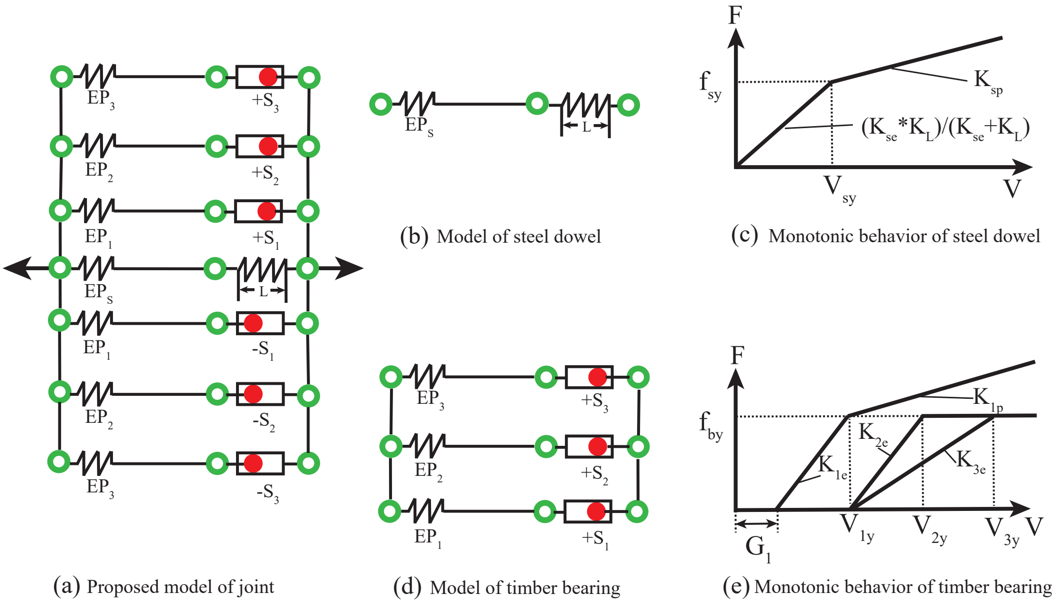


Figure 12: Modelling hysteretic behaviour of truss joints.

model a one-sided constraint of the joint as shown in Figure 12 for $+S_i$. When it is combined with other elements in series, it can model the initial sliding behavior caused by the tolerance between bolt and bolt hole. Here, the distance between the slider and the right end of the slot (upper limit) is set to be equal to the real manufacture tolerance, $G_1$. Based on the definition of $+S_1$, the EP and LOCK element connected to it can only achieve a net positive load under positive deformation. Similarly, the EP and LOCK element connected to $-S_i$ can only achieve a net negative load under negative deformation. It is proposed that the plasticity of the steel bolt ($EP_s$ ) is defined by kinematic hardening. The force that is contributed by the steel bolt under monotonic loading can therefore be calculated using the following equations:

$$F_s\,(V) = 0\,(V < G_1) \tag{27a}$$

$$F_s\,(V) = K_{se}K_L/\,(K_{se} + K_L) \cdot V\,(G_1 < V < V_{sy}) \tag{27b}$$

$$F_s\,(V) = K_{sp}\,(V - V_{sy}) + f_{sy}\,(V \geq V_{sy}) \tag{27c}$$

*3.2.2. Beam bearing model*

A combination of EP and S elements is used to model the bearing of the beam, as shown in Figure 12. As mentioned above, the S elements also model a one-sided constraint of the joint. Here, the distance between the slider and the right end of the slot (upper limit) is set to be equal to the gap width, $G_i\,(i = 1, 2, 3)$. The distance to the left end (lower limit) of the slot is set to be a large value which is impossible to reach (i.e., 30 mm). Details about the irrecoverable deformation of timber and the contact status between the steel bolt and the timber are retained by the S element.

Several assumptions are made for the timber bearing action model, namely (*i*) the yield strengths for $EP_1$, $EP_2$ and $EP_3$ are equal, (*ii*) $EP_2$ and $EP_3$ are elasto-perfect plastic, and (*iii*) the hardening rule for $EP_i$ $(i = 1, 2, 3)$ is delineated by isotropic hardening. With these assumptions, a gradual elasto-plastic transition stage of the force-slip curve can be achieved, and the loading and unloading stiffnesses can be set unequal to each other. Based on the model and assumptions described above, the moment of resistance generated by the timber bearing action can be calculated using the following equations:

$$F_b\left(V\right) = \Sigma F_i\left(V\right) \qquad (i = 1, 2, 3) \tag{28a}$$

$$F_i\left(V\right) = 0 \qquad (V < G_i) \tag{28b}$$

$$F_i\left(V\right) = K_{ie}\left(V - G_i\right) \qquad G_i < V < V_{iy} \tag{28c}$$

$$F_i\left(V\right) = K_{ip}\left(V - V_{iy}\right) + f_{by} \qquad V > V_{iy} \tag{28d}$$

where $F_i$ is the moment generated by the $i$-th timber model, $G_i$ is the gap of the $S_i$ element, $V_{iy}$ is the yield rotation of the $i$-th timber model, $K_{ie}$ is the elastic stiffness of the $EP_i$ element, $K_{ip}$ is the post-yield stiffness of the $EP_i$ element ($K_{2p} = K_{3p} = 0$), and $f_{by}$ is the yield strength of the $EP_i$ element.

### *3.3. Parametric modelling of truss joints via Python script*

Domain decomposition with overlapping node method is used to divide the simplified model into different subdomains. The multiple overlapping nodes between different subdomains constitute a coupling region, which could be easily integrated into hybrid structural model. Since overlapping nodes is unable to be captured in GUI interface of ABAQUS software, herein parametric modelling is performed via Python script to compile *Inp* file, where geometry, node coordinate, material property, boundary conditions, loading input and response output are defined. Parametric modeling is an approach to capture designs by parameters, which are defining objects by certain algorithms and mathematic procedures. This is in controversy to a direct draw and design. In this way multiple components can be introduced in a model and repetitive objects and overlapping nodes can be created easily, while still adopting to apparent environments. As displayed in Figure 13, a vector of integer values $j$ (Eq. 29c) from 1-7 is used to represented the sequence number of internodes in simplified joints model, while the overlapping start node and end node are represented by $N_{i0}$ and $N_{i2}$ respectively, where a vector of integer values $i$ (Eq. 29b) will be adopted to represent the sequence number of $n$ joints in global structure under consideration, herein are 6 global nodes of hybrid planar truss (see Figure 21).

After parametric modelling, the resulting *Inp* file is imported into ABAQUS software platform for FEM analysis without adopting ABAQUS GUI interface and this process can be totally operated via Python script:

$$N_{i1j}^{T} = [N_{i11}, N_{i12}, N_{i13}, N_{i14}, N_{i15}, N_{i16}, N_{i17}] \tag{29a}$$

$$i^{T} = [1, 2, 3......., n] \tag{29b}$$

$$j^{T} = [1, 2, 3, ..., 7] \tag{29c}$$

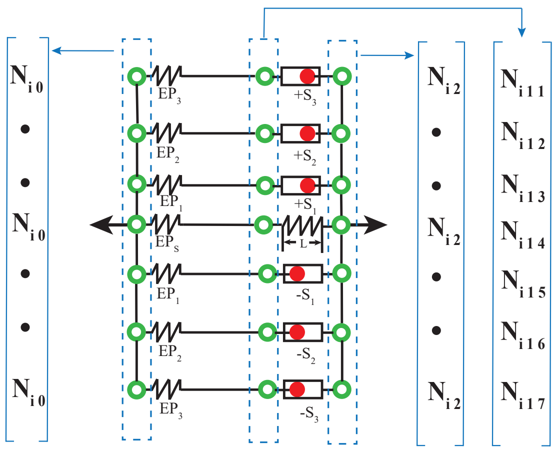


Figure 13: Node information in parametric modelling of truss joints.

### 3.4. Rough estimation of parameters

Preassigning values of certain parameters and defining a restricted searching space for parameters to be optimized (e.g., limiting the optimization to a portion of parameters instead of the whole) can dramatically reduce the computational cost of the calibration. Thus, it is critical to perform a rough estimation of parameters first, which involves extraction of the characteristic points and parameters of the hysteresis curves from the simulated results by 3D continuum FE model (i.e., the stiffness, $K$, and the yield slip, $V_y$). The definition of characteristic points and the rough determination of model parameters will be introduced in this section.

To solve all the unknown parameters, the initial stiffness, $K$, yield slip, $V_y$ and four characteristic points, $P_1$ , $P_2$ , $P_3$ and $P_4$ on the hysteresis curves of joint model are needed to be specified additionally, as shown in Figure 14. $P_1(V_1, F_1)$ and $P_2(V_2, F_2)$ are determined as the hardening-initiating point and peak-loading point respectively, which could be roughly estimated from the hardening segment of the hysteretic curve. $P_3(V_3, F_3)$ are determined as the intercept of the hysteresis curve on the $+x$ axis and $P_4(V_4, F_4)$ as the intercept of the hysteresis curve on the $-y$ axis, both of which could be roughly estimated from the unloading segment. Since more stable curves will result from repeated load cycles, it is suggested to define $P_3$ and $P_4$ in the last cycle.

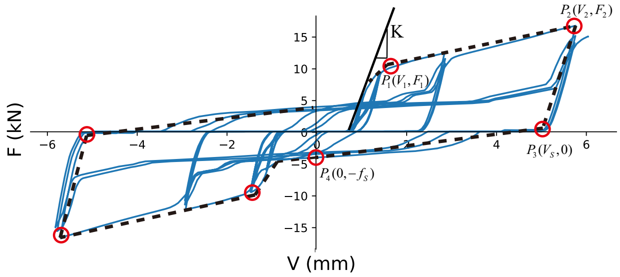


Figure 14: Selection of characteristic points on hysteresis curves for simplified model development.

The proposed method for roughly determining the parameters is defined by several steps, namely, $(i)$ the initial stiffness of the model $= K$, $(ii)$ the yielding of the steel bolt model $= V_y$, $(iii)$ the post-peak stiffness of the steel bolt model = the slope of the line $P_4$-$P_3$, $(iv)$ the yield strength of the steel bolt model $= f_s$ , and (v) the moment of the model is equal to that of the test results at $V = V_1$ and $V = V_2$. Additionally, it is proposed $G_2 = G_3 = G_1 + f_{by}/K_{1e}$, $V_{2y} = 0.5(V_1 + V_y)$ and $V_{3y} = V_1$, where $V_y$ is the yield rotation of the joint adopted from the test results. With these assumptions, the $EP_2$ and $EP_3$ elements can begin to work instantaneously after $EP_1$ yields, while the contribution of the timber bearing increases linearly according to slope $K_{1p}$ when the slip of the joint is greater than $V_1$. Yield of $EP_2$ and $EP_3$ can simulate the transition from the elastic stage to the post-yield stage.

Based on the conditions listed above, the following equations must therefore be satisfied:

$$\begin{gathered}
[(K_{se}K_L)\,/\,(K_{se} + K_L)] + K_{1e} = K \\
V_{sy} = V_y \\
K_{sp} = f_s/V_s \\
f_{sy} = f_s \\
F\left(V_1\right) = F_1 \\
F\left(V_2\right) = F_2
\end{gathered} \tag{30}$$

By substituting Eqs. 26, 27b and 27c into the above equations, the parameters of the steel bolt and beam bearing models can be calculated as follows:

- For the bolt model:

$$
\begin{aligned}
f_{sy} &= f_s \\
K_{sp} &= f_s/V_s \\
K_L &= \frac{f_{sy}K_{se}}{K_{se}V_y - f_{sy}}
\end{aligned}
\tag{31}
$$

- For the beam bearing model:

$$
\begin{aligned}
K_{1e} &= K - f_{sy}/V_y \\
K_{1p} &= \frac{F_2 - F_1}{V_2 - V_1} - K_{sp} \\
f_{by} &= \frac{F_2 - f_{sy} - V_2(K_{1p} + K_{sp}) + V_y K_{sp} - G_1 K_{1p}}{3 - K_{1p}/K_{1e} - G_1} \\
G_2 &= G_3 = f_{by}/K_{1e} \\
K_{2e} &= \frac{f_{by}}{0.5(V_y + V_1) - G_2 - G_1} \\
K_{3e} &= \frac{f_{by}}{V_1 - G_2 - G_1}
\end{aligned}
\tag{32}
$$

It is observed from the hysteresis curves that the initial loading stiffness is always smaller than the unloading stiffness. The lock element in the steel dowel model is hence applied herein to model this phenomenon. Among the above equations, there are two indeterminate parameters, $K_{se}$ and $K_L$, which can be solved by assuming one of the values. Through pilot parametric studies, when increasing the value of $K_{se}$, the arising unloading slope will be steeper although there is less effect on the dissipated energy. This observation was also noted in reference [12]. Therefore, the rough estimated values of $K_{se}$ is assumed to be 25 kN/mmin order to achieve a best fit to the unloading stiffnesses.

## 4. Model identification of low-fidelity connections based on high-fidelity model output

The proposed model holds a large number of flexible parameters. Hence, automatic parameter calibration is indispensable. This study presents a novel PGA based framework aimed at identifying parameters to minimize force-time history error between predicted hysteretic behavior from low-fidelity model and high fidelity models joints model (see Figure 14).

### *4.1. Parallel genetic algorithms (PGA) and parallel computing system*

Genetic algorithms (GA) are a discrete evolution strategy method which employs an iterative procedure on the basis of evolution of a design population over a selected number of generations [49, 50]. In each iteration of this procedure, the design population is first evaluated in conjunction with response and constraint function calculations performed for each design, and then a sequential application of the recombination, mutation and selection operators takes place to constitute the individuals of the next generation. GA are very suitable for many problems, but often require too much time and therefore may be disadvantageous. The most time-consuming operation within GA is the evaluation of the fitness function [16, 17]. Hence, an effective and adequate parallelization of the solution algorithm can be accomplished by creating multitasked regions in the GA source code for this step only, since fitness evaluation of the design population does not entail any inter-processor communication, and thus can be conducted concurrently by a number of threads in a parallel computing environment.

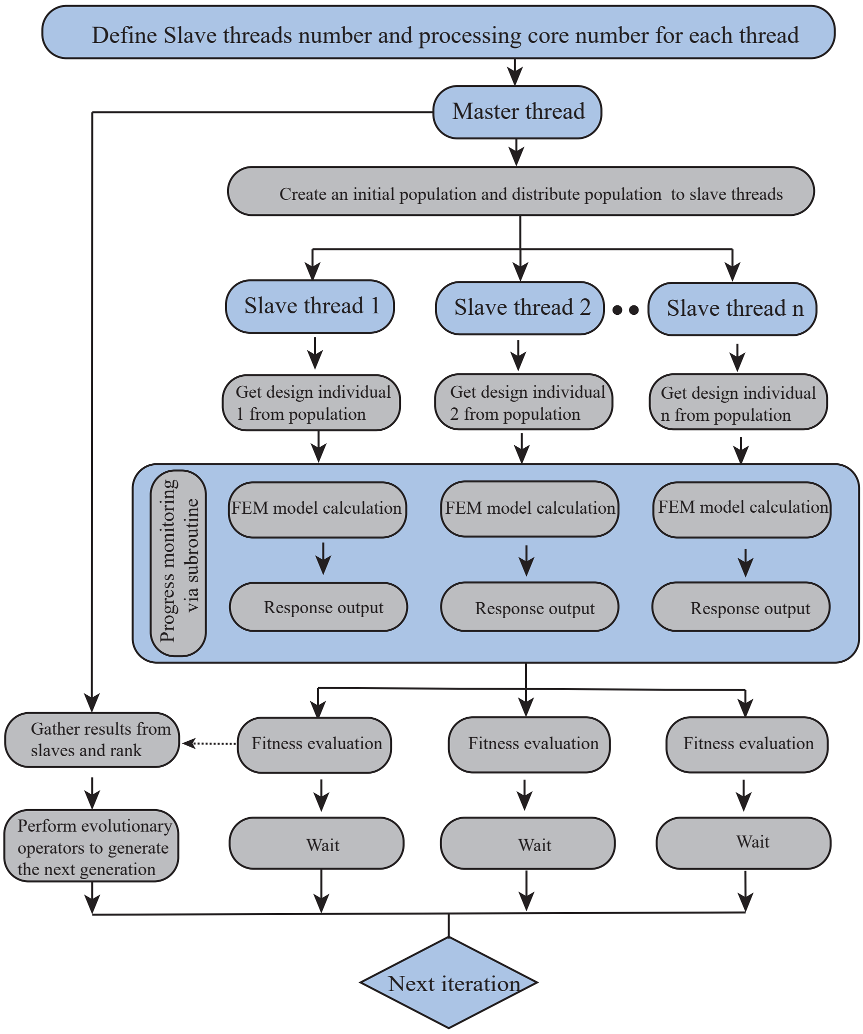


Figure 15: Flowchart for parallel genetic algorithm.

The serial algorithm is organized in a number of sequential and parallel code segments to achieve a master-slave configuration based parallel programming structure. The sequential code segments (recombination, mutation and selection) are only accessible by the master thread, whereas multitasked loops (FEM calculation and fitness evaluation) encapsulated in parallel codes are executed by slave threads. Additional sequential code segments are written for enabling coordination, communication and synchronization within the network by the master thread. The parallel execution of the solution algorithm is schematically depicted in Figure 15. Accordingly, once the algorithm is initiated, the input data describing the aforementioned parametric model (*Inp* file) is first distributed to all the slave threads by the master. Then, the initial population that, in the current case, represent different constitutive parameters of material model, is generated by the master thread based on a random initialization of parameters to be identified. Next, the master calls all the slave threads to perform evaluation of the design population collectively and concurrently. Each design (parametric model) is assigned to each slave thread within the parallel computing system by the master. Every thread undertakes FEM response calculations, response output and fitness evaluation calculations for the subset of designs assigned to itself in conjunction with ABAQUS platform. The results of analyses and evaluations are reflected in single numerical values, which are delivered from slave thread to the master as the objective function scores of the individuals. The master thread waits until every thread-in the parallel computing system completes its own task. It then continues to implement evolutionary operators in a sequential manner to yield the design population of the next generation, while slave threads are put on hold in the meantime until response and fitness evaluation calculations are processed in the next generation.

It is important to emphasize that progress monitoring of FEM calculation and response output in each thread is critical for parallelization and iteration execution. To solve this, each thread contains a self-monitoring subroutine, which monitor FEM calculation progress by judging existence of *lck* file and monitor response output progress by judging existence of post-processing output txt file.

### *4.2. Identification framework*

The parameter calibration framework proposed herein is based on the above-mentioned Parallel genetic algorithms (PGA) and parallel computing system. The flowchart of this calibration framework is depicted in Figure 16. The "Initial decision" allows preassigning values of certain parameters and defining a restricted searching space for parameters to be optimized. As it can be observed in Figure 16, the core of the framework is the identification algorithm. The algorithm involves the definition of a proper objective function that estimates the error between simulated force-time history from low-fidelity model and observed force-time history from high-fidelity FE model:

$$OF(\boldsymbol{\theta}) = \frac{\int_{v_0}^{v_f} |[\mathbf{F}_O(v) - \mathbf{F}_S(\boldsymbol{\theta}, v)]| \, \mathrm{d}v}{\int_{v_0}^{v_f} |\mathbf{F}_O(v)| \, \mathrm{d}v} \tag{33}$$

where $\boldsymbol{\theta} = \{K_{1e}, f_{by}, K_{1p}, K_{2e}, K_{3e}, G_1, G_2, K_L, f_{sy}, K_{se}, K_{sp}\}$ is the vector collecting the model parameter to be identified, $v_0$ and $v_f$ are the initial and final displacement records, $\mathbf{F}_O(v)$ is the force derived from the observed data from high-fidelity FE model, and $\mathbf{F}_S(\boldsymbol{\theta}, v)$ is the force simulated by the proposed low-fidelity model. The values of $\mathbf{F}_S(\boldsymbol{\theta}, v)$ is obtained by performing a cyclic analysis of proposed simplified model in ABAQUS platform in Python. Then the objective function value is mapped to fitness values and the fitness values of each tentative solution is evaluated. The fittest individuals are cyclically selected and recombined until the optimal parameters configuration are obtained.

Table 2: Rough estimation of parameters to be identified and the searching space.

| Parameters | $K_{1e}$ [kN/mm] | $f_{by}$ [kN] | $K_{1p}$ [kN/mm] | $K_{2e}$ [kN/mm] | $K_{3e}$ [kN/mm] | $G_1$ [mm] | $G_2$ [mm] | $K_L$ [kN/mm] | $f_{sy}$ [kN] | $K_{se}$ [kN/mm] | $K_{sp}$ [kN/mm] |
|---|---|---|---|---|---|---|---|---|---|---|---|
| Rough estimation | 28.8 | 4 | 0.414 | 1.66 | 5.26 | 0.8 | 0.14 | 1.25 | 5 | 25 | 1.19 |
| Upper Bound | 288 | 40 | 4.14 | 16.6 | 52.6 | 8 | 1.4 | 12.5 | 50 | 250 | 11.9 |
| Lower Bound | 0.576 | 0.08 | 0.008 | 0.033 | 0.105 | 0.016 | 0.003 | 0.025 | 0.1 | 0.5 | 0.024 |

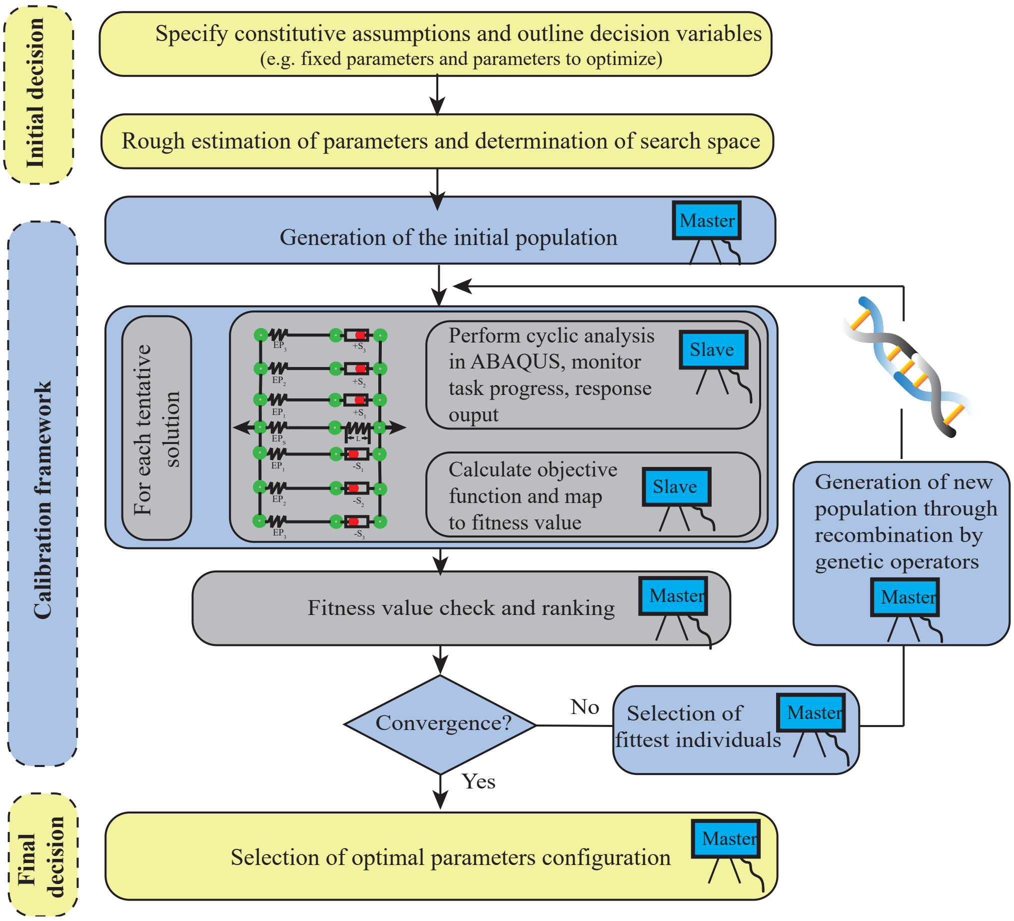


Figure 16: Flowchart of the calibration framework [51, 52].

### 4.3. Identification results

After rough determination of model parameters according to 3.4, an amplification factor 10 and a reduction factor 0.2 for rough estimation values of all the parameters are selected as the upper bound and lower bound of the searching space as reported in Table 2. The population size and generation number are chosen as 20 and 30, respectively. Thus, the identification process will perform a total of 600 times evaluation, where 20 slave threads are arranged to evaluate 20 individuals in each generation and 2 processors are distributed to execute each thread, as reported in Table 3.

Table 3: Setting of the PGA.

| Pop.size | N.Generation | Evaluation | N.Slave threads | N.cores per thread |
|---|---|---|---|---|
| 20 | 30 | 600 | 20 | 2 |

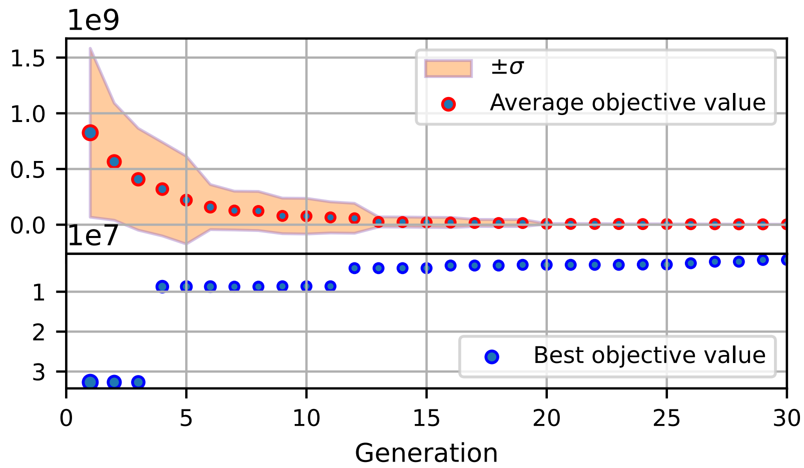


Figure 17: Convergence history of the identification over the objective function evalution.

Under the above settings, the identification process for the reference model has shown the convergence history illustrated in Figure 17, where the objective function evaluations are reported according to Eq. 33. In the same diagram, the moving average trend is also reported. It can be observed that the algorithm tends to a stable solution after about 8 generations, 160 evaluations of individuals.The final identification results over each individual in each generation are illustrated in Figure 18. A good agreement between predicted responses from proposed simplified model and benchmark response from 3D FEM model is achieved in the last generation and the final identified parameters are concluded in Table 4.

Table 4: Identified parameters of simplified model for truss joints.

| Parameters | $K_{1e}$ | $f_{by}$ | $K_{1p}$ | $K_{2e}$ | $K_{3e}$ | $G_1$ | $G_2$ | $K_L$ | $f_{sy}$ | $K_{se}$ | $K_{sp}$ |
|---|---|---|---|---|---|---|---|---|---|---|---|
| | [kN/mm] | [kN] | [kN/mm] | [kN/mm] | [kN/mm] | [mm] | [mm] | [kN/mm] | [kN] | [kN/mm] | [kN/mm] |
| Identified | 98.418 | 2.603 | 0.313 | 11.380 | 35.783 | 0.720 | 1.185 | 2.581 | 32.583 | 70.390 | 0.05 |

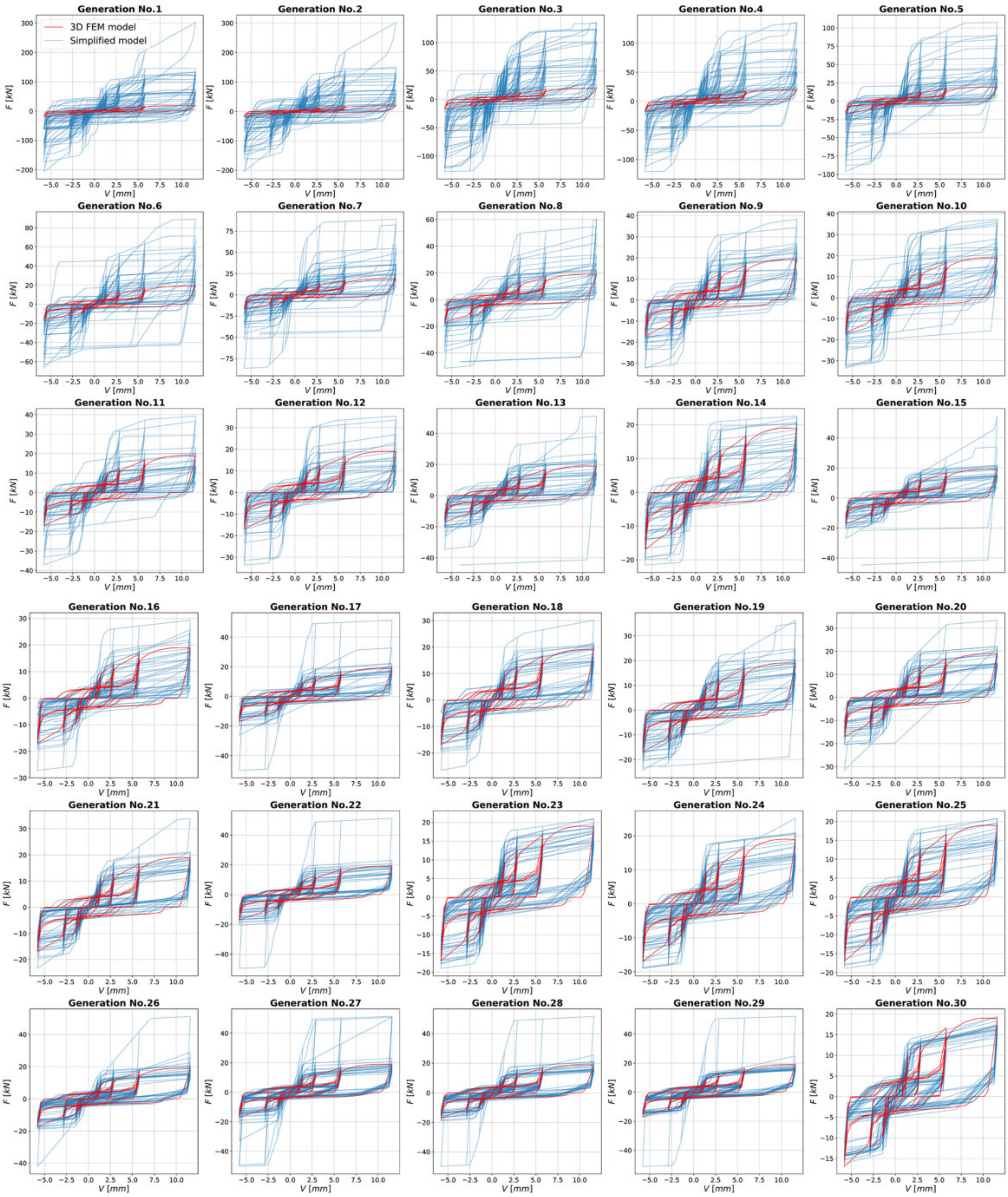


Figure 18: Identification results over each individual in each generation.

### 4.4. Comparison with other identification methods

The proposed PGA was compared with particle swarm optimization algorithm (PSO) [53], bayesian inference using Sequential Monte Carlo sampling method (BI-SMC) and successful history-based adaptive differential evolution algorithms with linear population size reduction (L-SHADE) [54]. The search space defined by the PSO and L-SHADE is consistent with that of the PGA, while truncnormal distribution with mean values equal to the roughly determined parameters values as discussed in section 3.4 was chosen as the prior distribution of BI-SMC. An amplification factor of 3.0 and a reduction factor of 0.1 for mean values of all the parameters are selected as the upper bound and lower bound of the *truncnormal* distribution. 0.5 times the mean values are selected as the standard deviations of the priors.

The predicted hysteresis response and energy dissipation-time history obtained by substituting the parameter values identified by the four identification methods into the simplified model was shown in Figure 19, and the predicted results by simplified model were further compared with the predicted results by 3D FEM model. To assess the discrepancy between predicted results by 3D FEM model and simplified model using identified parameter values by the four identification methods, two error metrics are employed: the Cumulative Energy Error (CEE) and the cumulative force error (CFE). These metrics are calculated as:

$$CEE_i = \frac{\mid E_{it} - E_{im} \mid}{\mid E_{it} \mid} \times 100\% \tag{34a}$$

$$CFE_i = \frac{\sum_{k=1}^{i} \mid F_{kt} - F_{km} \mid}{\sum_{k=1}^{i} \mid F_{kt} \mid} \times 100\% \tag{34b}$$

where $i$ is the i-th data point. $E_{it}$ and $E_{im}$ are the total energy dissipated up to the $i$-th point for test and model, respectively. $F_{kt}$ and $F_{km}$ are the force of the $k$-th point for test and model, respectively.

Figure 20 illustrated that the identification error was smallest when employing the L-SHADE method, followed by PGA and then PSO. The accuracies of PGA and PSO were similar, while the predictive accuracy of BI-SMC was lower than that of the other algorithms. In assessing the merits and drawbacks of different methodologies, it is inadequate to solely gauge identification accuracy. Identification efficiency holds significance as well. Thus, this study comprehensively evaluated the strengths and limitations of diverse approaches, considering factors such as identification accuracy and efficiency as shown in Table 5.

## 5. Model updating of an hybrid planar truss based on experimental tests

### 5.1. FE model

A simplified hybrid truss model is developed by combining the aforementioned simplified joints model with wire element (truss chords) in ABAQUS as shown in Figure 21. The simplified joint model (see Section 3) is located between the truss global node and wire element and its length is set as 120 mm, which represents real joints length (see Figure 1). Wire element is assigned with truss beam property, where the

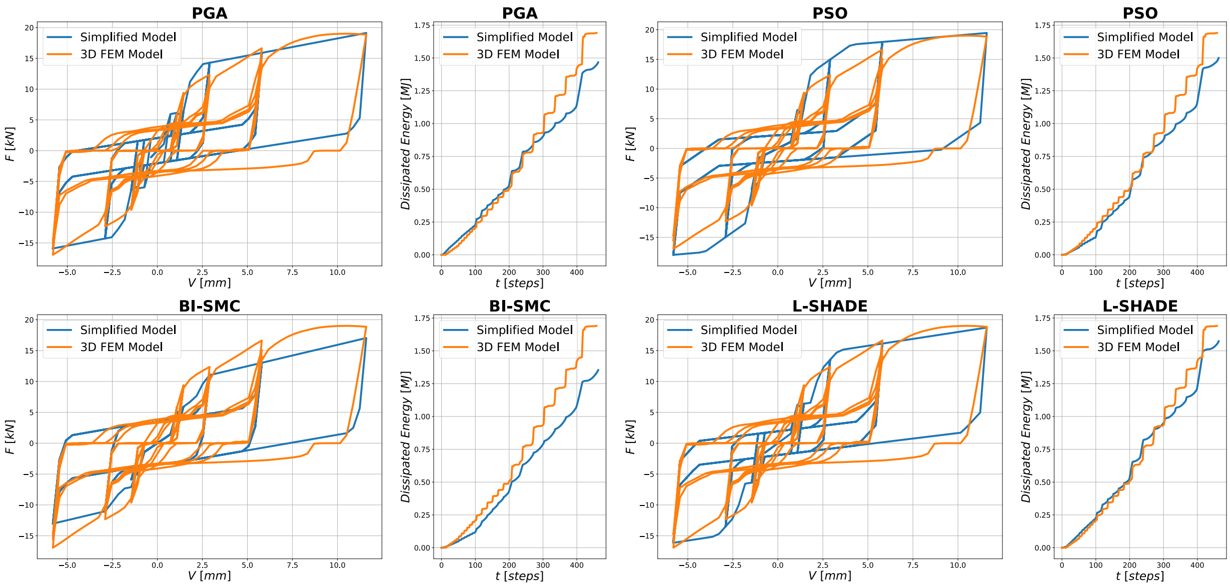


Figure 19: Comparison of identification results obtained by PGA and other identification methods regarding hysteresis response and energy dissipation.

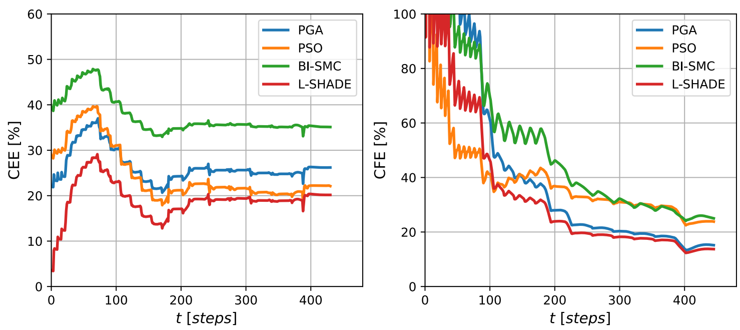


Figure 20: Comparison of the Cumulative Energy Error (CEE) and the Cumulative Force Error (CFE).

elastic modulus is 13 Gpa and section area is 60mm $\times$ 60mm. All the nodes are assumed as hinge connection and the support adopts pin connection, which complies with real boundary conditions. The model developed in ABAQUS is illustrated in Figure F.25 (b).

Table 5: Features of four methods and comparison.

| Method | PGA | PSO | BI-SMC | L-SHADE |
|---|---|---|---|---|
| Accuracy | Medium | Medium | Relatively low | High |
| Computation cost | Around 1 h | Around 70 h | Around 95 h | Around 44 h |
| Evaluation iteration | 600 | 600 | 2300 | 900 |
| Overall Efficiency | High | Low | Low | Medium |
| Level of Detail of Output | Deterministic | Deterministic | Probabilistic, with uncertainty | Deterministic |
| Stability | Unstable (largely depend on the initial population) | Unstable (largely depend on the initial population) | Stable (if you have a reasonable prior distribution) | Unstable (largely depend on the initial population) |
| Recommended Situations | Quick parameter estimation | Accurate parameter identification based on preliminary results | Uncertainty quantification of parameters | Accurate parameter identification based on preliminary results |

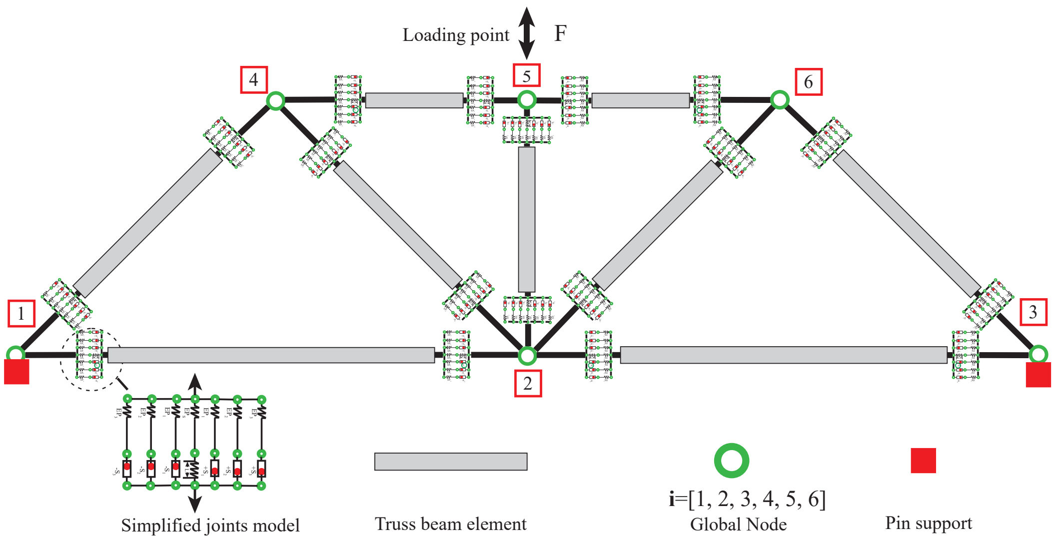


Figure 21: Simplified hybrid truss model in ABAQUS.

The overall nonlinear behavior of the simplified joints model is described by predicted hysteretic response according to aforementioned parameter identification results. However, it should be noted that this highly idealized structural model localizes the modeling of nonlinear behavior in a few prescribed elements, leading to potential model uncertainty. To address this model uncertainty and construct more robust structural models with more accurate parameters, a PGA based model updating framework is carried out. The benchmark of updating refers to a cyclic test result of real hybrid planar truss. The loading scenario of real hybrid planar truss is shown in Figure F.25 and 21, and displacement based cyclic loading is applied on node 5.

The flowchart of updating framework is similar to aforementioned identification framework with truss joints. The differences are the input parametric model and basic PGA setting. Considering truss model is more complicated than individual joint model, The iterative generation and population size is selected as

60 and 30, respectively, leading to a total of 1800 times evaluation, and 30 slave threads are assigned to undertake updating task. An amplification factor 5 and a reduction factor 0.5 assigned to initial parameter identification values of joints model are selected as the upper bound and lower bound of the searching space for hybrid truss updating.

### *5.2. Model updating results*

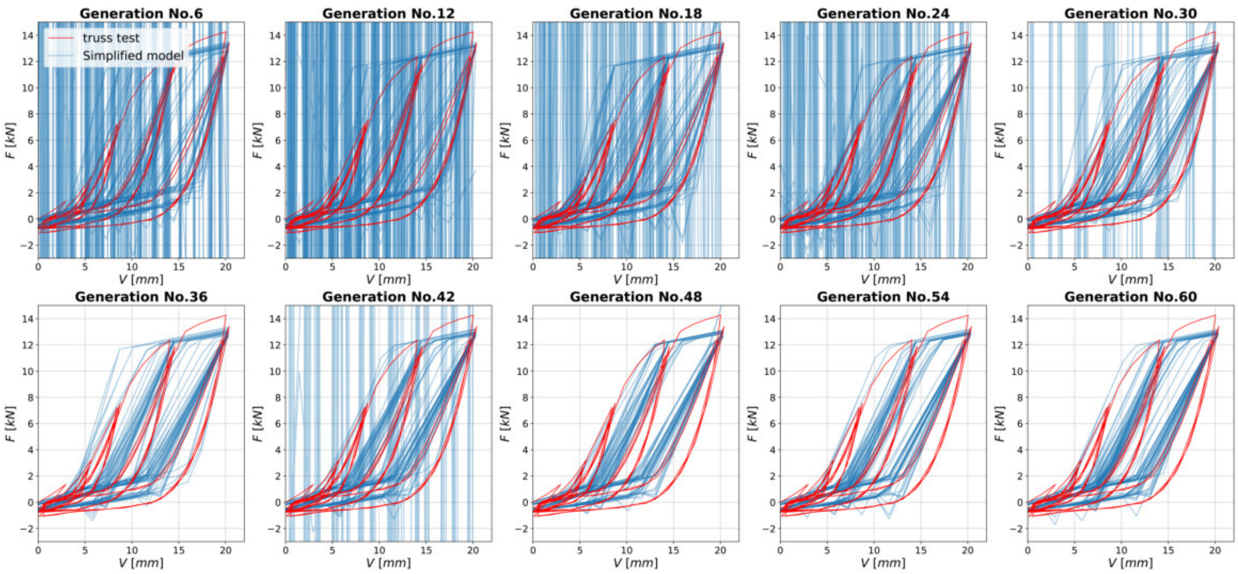


Figure 22: Model updating results over each individual in some generations.

Table 6: Identified parameter values from joints and updated parameters values from hybrid planar truss.

| Parameters | $K_{1e}$ | $f_{by}$ | $K_{1p}$ | $K_{2e}$ | $K_{3e}$ | $G_1$ | $G_2$ | $K_L$ | $f_{sy}$ | $K_{se}$ | $K_{sp}$ |
|---|---|---|---|---|---|---|---|---|---|---|---|
| | [kN/mm] | [kN] | [kN/mm] | [kN/mm] | [kN/mm] | [mm] | [mm] | [kN/mm] | [kN] | [kN/mm] | [kN/mm] |
| Initially identified | 98.418 | 2.603 | 0.313 | 11.380 | 35.783 | 0.720 | 1.185 | 2.581 | 32.583 | 70.390 | 0.05 |
| Finally Updated | 84.312 | 2.351 | 0.421 | 13.621 | 27.412 | 1.211 | 1.701 | 2.124 | 27.654 | 63.392 | 0.07 |
| Relative Error | 14% | 9.7% | 34.5% | 19.7% | 23.4% | 68.19% | 43.54% | 17.7% | 15.1% | 9.7% | 40% |

The updating process for the truss model has shown the convergence history illustrated in Figure 23, where the objective function evaluations are reported, and the model updating results over each individual in some representative generations are shown in Figure 22. It can be observed that the updating tends to a stable solution after about 48 generations, 1440 evaluations of individuals. A good agreement between predicted responses and test responses is achieved in the last generation. The initially identified parameters, the finally updated parameters values and their relative error are reported in Table 6. As indicated, the most sensitive parameters are $G_1$ and $G_2$ from STOP behavior in $S$ element, which can characterize the initial slip behavior caused by the manufacture tolerance between bolt and hole wall. Since planar truss are composed of multiple chords and manufacture tolerance are difficult to keep uniform, these two parameters have the largest relative error between initially identified values and finally updated values.

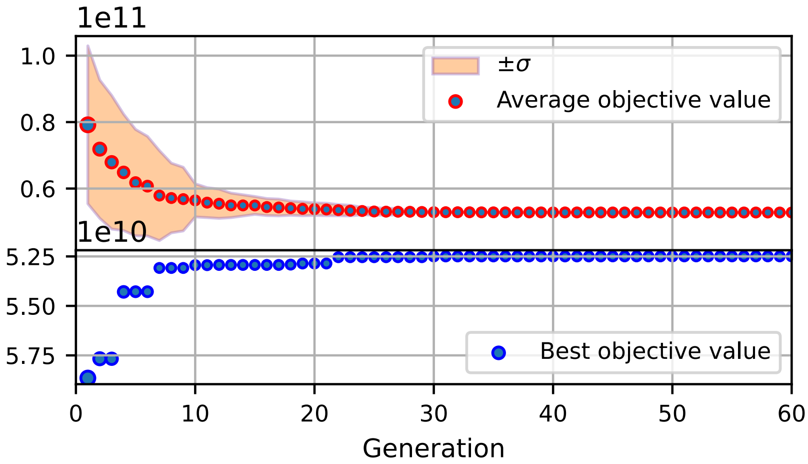


Figure 23: Convergence history of the updating over the objective function evaluation.

## 6. Conclusions

This study has addressed significant challenges in the modeling of bio-based connection systems, specifically for bolted steel to Laminated Veneer Lumber (LVL) and glued laminated bamboo (glubam) structures. Through the development of a 3D continuum FE model, integrated within ABAQUS, we have demonstrated a novel approach to accurately simulate the complex, orthotropic behavior of these materials. Our model incorporates the Hill yield criterion and an element removal technique, advancing the current understanding of how these materials respond under varying stress conditions, particularly focusing on their susceptibility to fracture. The integration of advanced joint modeling techniques with low-fidelity elements within ABAQUS offered a more reliable and computationally efficient method for predicting the performance of bio-based truss systems.

Moreover, the implementation of a multi-threaded parallel analysis and genetic algorithms within our FE model updating framework has proven essential. This approach enhances the accuracy of model predictions with reasonable computational time, aligning them closely with observed structural responses. This alignment is crucial to optimize and validate complex structural analyses, ensuring that the models perform accurately under real-world conditions. In conclusion, our research provides a significant advancement in the field of structural engineering, offering new tools and methodologies that improve the predictability and reliability of bio-based connection systems. These developments not only contribute to the body of knowledge but also have practical implications for the design and analysis of sustainable construction materials, thereby supporting the broader adoption of bio-based materials in engineering applications.

## Acknowledgments

Da Shi is mainly supported by China Scholarship Council (CSC). This research is supported by the National Key Research and Development Program of China (2019YFD1101002). This work has been partially supported by the Zhejiang University/University of Illinois at Urbana-Champaign Institute.

## CRediT

S. Da: Writing - Original Draft, Methodology, Conceptualization, Formal analysis, Investigation. Giuseppe Carlo Marano: Supervision, Formal analysis, Methodology, Conceptualization, Writing - Review & Editing. C. Demartino: Supervision, Formal analysis, Methodology, Conceptualization, Writing - Review & Editing;

## Declaration of Competing Interest

The authors declare that they have no known competing financial interests or personal relationships that could have appeared to influence the work reported in this paper.

## Data availability

The data that support the findings of this study are available from the corresponding author, C.D., upon reasonable request.

## References

[1] M. H. Ramage, H. Burridge, M. Busse-Wicher, G. Fereday, T. Reynolds, D. U. Shah, G. Wu, L. Yu, P. Fleming, D. Densley-Tingley, et al., The wood from the trees: The use of timber in construction, Renewable and Sustainable Energy Reviews 68 (2017) 333–359.

[2] T. Reynolds, B. Sharma, K. Harries, M. Ramage, Dowelled structural connections in laminated bamboo and timber, Composites Part B: Engineering 90 (2016) 232–240.

[3] L.-M. Ottenhaus, R. Jockwer, D. van Drimmelen, K. Crews, Designing timber connections for ductility–a review and discussion, Construction and Building Materials 304 (2021) 124621.

[4] S. Wang, H. Li, G. Cheng, Z. Xiong, M. Ashraf, Mechanical behavior of bolted steel laminated bamboo lumber connections loaded perpendicular to grain, Construction and Building Materials 345 (2022) 128302.

[5] J. A. Huber, M. Ekevad, U. A. Girhammar, S. Berg, Structural robustness and timber buildings–a review, Wood Material Science & Engineering 14 (2019) 107–128.

[6] B. Madsen, Reliable timber connections, Progress in Structural Engineering and Materials 1 (1998) 245–252.

[7] F. Wang, J. Yang, Experimental and numerical investigations on load-carrying capacity of dowel-type bolted bamboo joints, Engineering Structures 209 (2020) 109952.

[8] X. Zhang, Y. Sheng, E. Zhao, H. Yin, S. Li, S. Li, Q. Liu, Experiment and finite element analysis on load-carrying performance of double-shear connections of inorganic-bonded bamboo composite, Journal of Building Engineering (2024) 108756.

[9] B.-H. Xu, A. Bouchaïr, M. Taazount, E. J. Vega, Numerical and experimental analyses of multiple-dowel steel-to-timber joints in tension perpendicular to grain, Engineering Structures 31 (2009) 2357–2367.

[10] Z. Guan, P. D. Rodd, Hollow steel dowels — a new application in semi-rigid timber connections, Engineering Structures 23 (2001) 110–119.

[11] L. F. Sirumbal-Zapata, C. Málaga-Chuquitaype, A. Y. Elghazouli, A three-dimensional plasticity-damage constitutive model for timber under cyclic loads, Computers and Structures 195 (2018) 47–63.

[12] M. Izzi, A. Polastri, M. Fragiacomo, Investigating the hysteretic behavior of cross-laminated timber wall systems due to connections, Journal of Structural Engineering-asce 144 (2018) 04018035.

[13] C. Bedon, M. Fragiacomo, Numerical analysis of timber-to-timber joints and composite beams with inclined self-tapping screws, Composite Structures (2019).

[14] J.-H. Chou, J. Ghaboussi, Genetic algorithm in structural damage detection, Computers & structures 79 (2001) 1335–1353.

[15] C. Koh, Genetic algorithms in structural identification and damage detection, in: Intelligent computational paradigms in earthquake engineering, IGI Global, 2007, pp. 316–341.

[16] V. Skorpil, V. Oujezsky, P. Cika, M. Tuleja, Parallel processing of genetic algorithms in python language, in: 2019 PhotonIcs and Electromagnetics Research Symposium, 2019, pp. 3727–3731.

[17] O. Hasançebi, T. Bahçecioğlu, Ö. Kurç, M. Saka, Optimum design of high-rise steel buildings using an evolution strategy integrated parallel algorithm, Computers & Structures 89 (2011) 2037–2051.

[18] T. Harada, E. Alba, Parallel genetic algorithms: a useful survey, ACM Computing Surveys (CSUR) 53 (2020) 1–39.

[19] E. Cantu-Paz, D. E. Goldberg, Efficient parallel genetic algorithms: theory and practice, Computer methods in applied mechanics and engineering 186 (2000) 221–238.

[20] Z. Konfrst, Parallel genetic algorithms: Advances, computing trends, applications and perspectives, in: 18th International Parallel and Distributed Processing Symposium, 2004. Proceedings., IEEE, 2004, p. 162.

[21] V.-T. Tran, T.-K. Nguyen, H. Nguyen-Xuan, M. A. Wahab, Vibration and buckling optimization of functionally graded porous microplates using bcmo-ann algorithm, Thin-Walled Structures 182 (2023) 110267.

[22] T. Sang-To, H. Le-Minh, M. A. Wahab, C.-L. Thanh, A new metaheuristic algorithm: Shrimp and goby association search algorithm and its application for damage identification in large-scale and complex structures, Advances in Engineering Software 176 (2023) 103363.

[23] T. Nghia-Nguyen, M. Kikumoto, H. Nguyen-Xuan, S. Khatir, M. A. Wahab, T. Cuong-Le, Optimization of artificial neutral networks architecture for predicting compression parameters using piezocone penetration test, Expert Systems with Applications 223 (2023) 119832.

[24] H.-L. Minh, S. Khatir, R. V. Rao, M. Abdel Wahab, T. Cuong-Le, A variable velocity strategy particle swarm optimization algorithm (vvs-pso) for damage assessment in structures, Engineering with Computers 39 (2023) 1055–1084.

[25] L. V. Ho, T. T. Trinh, G. De Roeck, T. Bui-Tien, L. Nguyen-Ngoc, M. A. Wahab, An efficient stochastic-based coupled model for damage identification in plate structures, Engineering Failure Analysis 131 (2022) 105866.

[26] P. Racher, K. Laplanche, D. Dhima, A. Bouchaïr, Thermo-mechanical analysis of the fire performance of dowelled timber connection, Engineering Structures 32 (2010) 1148–1157.

[27] M. Audebert, D. Dhima, M. Taazount, A. Bouchaïr, Numerical investigations on the thermo-mechanical behavior of steel-to-timber joints exposed to fire, Engineering Structures 33 (2011) 3257–3268.

[28] GB50005, Code for design of timber structures, 2017.

[29] D. Shi, Z. Li, C. Demartino, Bio-based hybrid planar truss: Experimental testing, fe modeling and bayesian model updating, Engineering Structures 308 (2024) 117987.

[30] G. Tang, L. Yin, Z. Li, Y. Li, L. You, Structural behaviors of bolted connections using laminated bamboo and steel plates, Structures 20 (2019) 324–339.

[31] C. Hong, H. Li, Z. Xiong, R. Lorenzo, X. Li, Z. Wang, Axial compressive behavior of laminated bamboo lumber columns with a chamfered section, Structures 33 (2021) 678–692.

[32] J. Jasieńko, T. Nowak, D. Czepiżak, Numerical analysis of cfrp-reinforced wooden beams under bending, volume 1, 2010.

[33] B.-H. Xu, A. Bouchair, P. Racher, Mechanical behavior and modeling of dowelled steel-to-timber moment-resisting connections, Journal of Structural Engineering 141 (2014) 04014165.

[34] R. Hill, A theory of the yielding and plastic flow of anisotropic metals, Proceedings of the Royal Society of London. Series A. Mathematical and Physical Sciences 193 (1948) 281 – 297.

[35] E. Jalilifar, M. G. Koliou, W. Pang, Experimental and numerical characterization of monotonic and cyclic performance of cross-laminated timber dowel-type connections, Journal of Structural Engineering (2021).

[36] B.-H. Xu, A. Bouchaïr, P. Racher, Analytical study and finite element modelling of timber connections with glued-in rods in bending, Construction and Building Materials 34 (2012) 337–345.

[37] B.-H. Xu, A. Bouchaïr, M. Taazount, P. Racher, Numerical 3d finite element modelling and experimental tests of rounded dovetail connection, European journal of environmental and civil engineering 17 (2013) 564–578.

[38] Z. Guan, E. Zhu, Finite element modelling of anisotropic elasto-plastic timber composite beams with openings, Engineering Structures 31 (2009) 394–403.

[39] H. Wen, H. Mahmoud, Strength determination and fracture characteristics of bolted connections, Journal of Structural Engineering 147 (2021) 04021132.

[40] H. Wen, H. Mahmoud, Block shear strength of coped beam connections with double bolt lines, Journal of Structural Engineering 148 (2022) 04021222.

[41] M. Yurrita, J. M. Cabrero, On the need of distinguishing ductile and brittle failure modes in timber connections with dowel-type fasteners, Engineering Structures 242 (2021) 112496.

[42] P. J. Gustafsson, Mean stress approach and initial crack approach, Fracture mechanics models for analysis of timber beams with a hole or a notch—a report of RILEM TC-133. Report TVSM-7134, Lund University, Sweden (2002).

[43] J. Zhang, M. He, Z. Li, Mechanical performance assessment of bolted glulam joints with local cracks, Journal of Materials in Civil Engineering 30 (2018) 04018094.

[44] D. Shi, H. Huang, N. Li, Y. Liu, C. Demartino, Bolted steel to laminated timber and glubam connections: Axial behavior and finite-element modeling, International Journal of Mechanical Sciences 252 (2023) 108364.

[45] J.-P. Hong, D. Barrett, Three-dimensional finite-element modeling of nailed connections in wood, Journal of Structural Engineering 136 (2010) 715–722.

[46] J. Zhang, M.-J. He, Z. Li, Numerical analysis on tensile performance of bolted glulam joints with initial local cracks, Journal of Wood Science 64 (2018) 364–376.

[47] M. He, J. Luo, D. Tao, Z. Li, Y. Sun, G. He, Rotational behavior of bolted glulam beam-to-column connections with knee brace, Engineering Structures 207 (2020) 110251.

[48] D. Shi, C. Demartino, Z. Li, Y. Xiao, Axial load–deformation behavior and fracture characteristics of bolted steel to laminated timber and glubam connections, Composite Structures 305 (2023) 116486.

[49] G. C. Marano, G. Quaranta, J. Avakian, A. Palmeri, Identification of passive devices for vibration control by evolutionary algorithms, 2013.

[50] R. Greco, J. Avakian, G. Marano, A comparative study on parameter identification of fluid viscous dampers with different models, Archive of Applied Mechanics 84 (2014).

[51] G. Quaranta, G. C. Marano, R. Greco, G. Monti, Parametric identification of seismic isolators using differential evolution and particle swarm optimization, Applied Soft Computing 22 (2014) 458–464.

[52] M. Pelliciari, G. Marano, T. Cuoghi, B. Briseghella, D. Lavorato, A. Tarantino, Parameter identification of degrading and pinched hysteretic systems using a modified bouc–wen model, Structure and Infrastructure Engineering 14 (2018) 1–13.

[53] H.-L. Minh, S. Khatir, R. V. Rao, M. A. Wahab, T. Cuong-Le, A variable velocity strategy particle swarm optimization algorithm (vvs-pso) for damage assessment in structures, ENGINEERING WITH COMPUTERS 39 (2023) 1055–1084.

[54] N. H. Awad, M. Z. Ali, P. N. Suganthan, R. G. Reynolds, An ensemble sinusoidal parameter adaptation incorporated with l-shade for solving cec2014 benchmark problems, 2016 IEEE Congress on Evolutionary Computation (CEC) (2016) 2958–2965.

## Appendix A. Detailed linear-elastic compliance tensor and stiffness tensor for orthotropic materials

The matrices $C^e$ and $D^e$ represent the compliance and stiffness tensors respectively for orthotropic materials, typically used in structural analysis for materials like laminated timber or other engineered wood products, which exhibit different properties along different axes. These tensors are crucial in understanding the behavior of such materials under load.

='The compliance matrix $C^e$, expressed in Voigt's notation, is a 6×6 matrix that simplifies the description of the elastic behavior of an orthotropic material. The entries in the matrix are dependent on the material's elastic moduli $E_1$, $E_2$, $E_3$ along three orthogonal axes, and the shear moduli $G_{12}$, $G_{13}$, $G_{23}$, as well as the Poisson's ratios $\mu_{ij}$ which describe the ratio of strains in perpendicular directions due to an applied stress:

$$C^e = \begin{bmatrix} \frac{1}{E_1} & \frac{-\mu_{21}}{E_2} & \frac{-\mu_{31}}{E_3} & 0 & 0 & 0 \\ \frac{-\mu_{12}}{E_1} & \frac{1}{E_2} & \frac{-\mu_{32}}{E_3} & 0 & 0 & 0 \\ \frac{-\mu_{13}}{E_1} & \frac{-\mu_{23}}{E_2} & \frac{1}{E_3} & 0 & 0 & 0 \\ 0 & 0 & 0 & \frac{1}{G_{12}} & 0 & 0 \\ 0 & 0 & 0 & 0 & \frac{1}{G_{13}} & 0 \\ 0 & 0 & 0 & 0 & 0 & \frac{1}{G_{23}} \end{bmatrix} \tag{A.1}$$

The inverse of the compliance matrix is the stiffness matrix $D^e$, which represents the material's ability to resist deformation under applied loads. This matrix is also expressed in Voigt's notation as a 6x6 matrix. The derivation of the stiffness matrix from the compliance matrix involves calculating the determinant $\Delta$ of a system derived from the interrelationships between the Poisson's ratios and the elastic moduli:

$$\Delta = 1 - \mu_{12}\mu_{21} - \mu_{23}\mu_{32} - \mu_{13}\mu_{31} - 2\mu_{21}\mu_{32}\mu_{13} \tag{A.2}$$

The fourth-order orthotropic linear elastic stiffness tensor $D^e$ is given by:

$$D^e = \begin{bmatrix} \frac{E_1(1-\mu_{23}\mu_{32})}{\Delta} & \frac{E_1(\mu_{21}+\mu_{31}\mu_{23})}{\Delta} & \frac{E_1(\mu_{31}+\mu_{21}\mu_{32})}{\Delta} & 0 & 0 & 0 \\ \frac{E_2(\mu_{12}+\mu_{32}\mu_{13})}{\Delta} & \frac{E_2(1-\mu_{13}\mu_{31})}{\Delta} & \frac{E_2(\mu_{32}+\mu_{12}\mu_{31})}{\Delta} & 0 & 0 & 0 \\ \frac{E_3(\mu_{13}+\mu_{23}\mu_{12})}{\Delta} & \frac{E_3(\mu_{23}+\mu_{13}\mu_{21})}{\Delta} & \frac{E_3(1-\mu_{12}\mu_{21})}{\Delta} & 0 & 0 & 0 \\ 0 & 0 & 0 & G_{12} & 0 & 0 \\ 0 & 0 & 0 & 0 & G_{23} & 0 \\ 0 & 0 & 0 & 0 & 0 & G_{31} \end{bmatrix} \tag{A.3}$$

## Appendix B. Matrix form of constitutive law for Hill's yield criterion in orthotropic material

The stress and strain vectors for engineering analysis in orthotropic materials, represented in Voigt notation, are essential for defining the material's response under various loading conditions. The stress vector $\{\sigma\}$ and the strain vector $\{\varepsilon\}$ are expressed as follows:

$$\{\sigma\} = \left\{ \begin{array}{cccccc} \sigma_{11} & \sigma_{22} & \sigma_{33} & \sigma_{12} & \sigma_{23} & \sigma_{31} \end{array} \right\} \tag{B.1a}$$

$$\{\varepsilon\} = \left\{ \begin{array}{cccccc} \varepsilon_{11} & \varepsilon_{22} & \varepsilon_{33} & r_{12} & r_{23} & r_{31} \end{array} \right\} \tag{B.1b}$$

Equations are developed to capture the dynamic relationship between stress and strain, incorporating the elastic and plastic behavior of the material:

$$\{d\sigma\} = \left( [D]^e - \frac{[D]^e \left\{\frac{\partial f}{\partial \sigma}\right\} \left\{\frac{\partial f}{\partial \sigma}\right\}^T [D]^e}{\frac{1}{h} + \left\{\frac{\partial f}{\partial \sigma}\right\}^T D^e \left\{\frac{\partial f}{\partial \sigma}\right\}} \right) (d\varepsilon) \tag{B.2}$$

where $[D]^e$ is reported in Eq. A.3. The elasto-plastic stiffness matrix $[D]$ is defined as follows:

$$[D] = [D]^e - \frac{[D]^e \left\{\frac{\partial f}{\partial \sigma}\right\} \left\{\frac{\partial f}{\partial \sigma}\right\}^T [D]^e}{\frac{1}{h} + \left\{\frac{\partial f}{\partial \sigma}\right\}^T [D]^e \left\{\frac{\partial f}{\partial \sigma}\right\}} \tag{B.3}$$

The yield function is modified to account for anisotropic behavior, described by the $\alpha_{ij}$:

$$\left\{\frac{\partial f}{\partial \sigma}\right\} = \frac{1}{2\overline{\sigma}} \begin{bmatrix} \alpha_{11}\sigma_{11} - \alpha_{12}\sigma_{22} - \alpha_{31}\sigma_{33} \\ -\alpha_{12}\sigma_{11} + \alpha_{22}\sigma_{22} - \alpha_{23}\sigma_{33} \\ -\alpha_{31}\sigma_{11} - \alpha_{23}\sigma_{22} + \alpha_{33}\sigma_{33} \\ 6\alpha_{44}\sigma_{12} \\ 6\alpha_{55}\sigma_{23} \\ 6\alpha_{66}\sigma_{31} \end{bmatrix} = \frac{1}{2\overline{\sigma}} \{B\} \tag{B.4}$$

where $B$ represents the vector of partial derivatives. $\{\phi\}$ denotes the product of $[D]^e$ and $\{B\}$ such as:

$$[D]^e \left\{\frac{\partial f}{\partial \sigma}\right\} = [D]^e \frac{1}{2\overline{\sigma}} \{B\} = \frac{1}{2\overline{\sigma}} \{\phi\} \tag{B.5}$$

where $\overline{\sigma}$ is the effective stress at initial yield.

In the yield function, let us assume that:

$$\alpha_{11} = \alpha_{12} + \alpha_{31}, \alpha_{22} = \alpha_{12} + \alpha_{23}, \alpha_{33} = \alpha_{23} + \alpha_{31} \tag{B.6}$$

Adopting Eq. B.6 and substituting these into the elasto-plastic stiffness matrix equation gives:

$$[D]^e \left\{\frac{\partial f}{\partial \sigma}\right\} = [D]^e \frac{1}{2\overline{\sigma}} \{B\} = \frac{1}{2\overline{\sigma}} \{\phi\} \tag{B.7}$$

Substituting these into the elasto-plastic stiffness matrix equation gives:

$$[D] = [D]^e - \frac{\{\phi\} \{\phi\}^T}{\{B\}^T \{\phi\} + 4\overline{\sigma}^2 \overline{H}} \tag{B.8}$$

where $\overline{H}$ is the hardening modulus. The term $\overline{\sigma}^2 \overline{H}$ helps adjust the influence of the material's hardening behavior on the overall stiffness matrix calculation.

This refined model captures the nuanced interactions between stress and strain in orthotropic materials. The procedure for the determination of anisotropic parameters $\alpha_{ij}$ is discussed in Appendix C.

## Appendix C. Determination of anisotropic parameters

The Hill yield criterion provides a systematic approach for determining the anisotropic parameters of a material based on experimental yield stresses obtained under simple tension and shear along the material's principal axes. This criterion adapts well to orthotropic materials, which exhibit different strengths and behaviors depending on the direction of the load.

Given the effective stress at initial yield, $\overline{\sigma}_0$, which is typically selected based on the yield stress in a reference direction (e.g., $\overline{\sigma}_0 = \sigma_{011}$ if direction 1 is chosen as the reference), the parameters $\alpha_{i,j}$ are calculated based on yield stresses ($\sigma_{0ij}$) obtained from experimental tests. These tests measure the initial yield stress under compression or shear in different principal directions:

$$\begin{array}{ccccc} \alpha_{13} + \alpha_{31} = 2\left(\frac{\overline{\sigma}_0}{\sigma_{011}}\right)^2 & , & \alpha_{13} + \alpha_{23} = 2\left(\frac{\overline{\sigma}_0}{\sigma_{022}}\right)^2 & , & \alpha_{23} + \alpha_{31} = 2\left(\frac{\overline{\sigma}_0}{\sigma_{033}}\right)^2 \\ \alpha_{44} = \frac{1}{3}\left(\frac{\overline{\sigma}_0}{\sigma_{012}}\right)^2 & , & \alpha_{55} = \frac{1}{3}\left(\frac{\overline{\sigma}_0}{\sigma_{023}}\right)^2 & , & \alpha_{66} = \frac{1}{3}\left(\frac{\overline{\sigma}_0}{\sigma_{031}}\right)^2 \end{array} \tag{C.1}$$

To derive individual values for each $\alpha_{i,j}$, the equations can be solved simultaneously. This involves algebraic manipulation to isolate each term, taking into account the interaction between different directions as influenced by the orthotropic nature of the material:

$$
\begin{aligned}
\alpha_{12} &= \left(\frac{\overline{\sigma}_0}{\sigma_{011}}\right)^2 + \left(\frac{\overline{\sigma}_0}{\sigma_{022}}\right)^2 - \left(\frac{\overline{\sigma}_0}{\sigma_{033}}\right)^2 \quad ; \quad \alpha_{44} = \frac{1}{3}\left(\frac{\overline{\sigma}_0}{\sigma_{012}}\right)^2 \\
\alpha_{23} &= -\left(\frac{\overline{\sigma}_0}{\sigma_{011}}\right)^2 + \left(\frac{\overline{\sigma}_0}{\sigma_{022}}\right)^2 + \left(\frac{\overline{\sigma}_0}{\sigma_{033}}\right)^2 \quad ; \quad \alpha_{55} = \frac{1}{3}\left(\frac{\overline{\sigma}_0}{\sigma_{023}}\right)^2 \\
\alpha_{31} &= \left(\frac{\overline{\sigma}_0}{\sigma_{011}}\right) - \left(\frac{\overline{\sigma}_0}{\sigma_{022}}\right)^2 + \left(\frac{\overline{\sigma}_0}{\sigma_{033}}\right)^2 \quad ; \quad \alpha_{66} = \frac{1}{3}\left(\frac{\overline{\sigma}_0}{\sigma_{031}}\right)^2
\end{aligned}
\tag{C.2}
$$

This method provides a robust framework for adjusting material models to reflect real-world behaviors based on empirical data.

## Appendix D. Plasticity-fracture constitutive model algorithm

## Appendix E. Test setup for truss joints

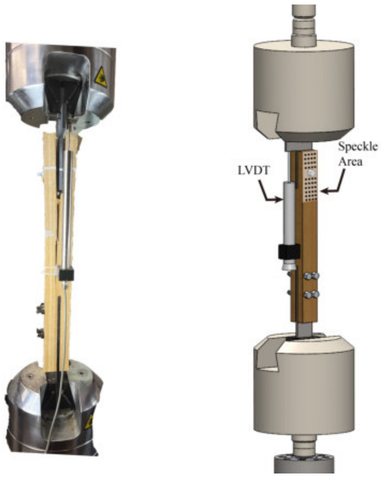


(a) (b)

Figure E.24: Test setup for truss joints and instrumentation: photo (a) and detail of the instrumentation (b)

## Appendix F. Test setup of the truss and FE model

(a) test on truss

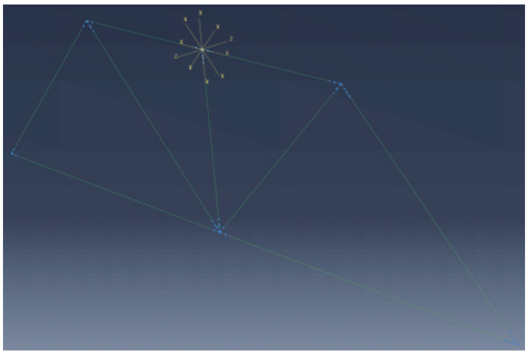

(b) truss model in ABAQUS

Figure F.25: Photo of the experimental setup of the planar truss structure (a) and truss model in ABAQUS (b).

Table D.7: Plasticity-fracture constitutive model algorithm for the beam material.

Initial values: $\varepsilon_0 = 0; \varepsilon_0^p = 0; \sigma_0 = 0$

Input material parameters: Materials constants $\{E_1, E_2, E_3, \mu_{12}, \mu_{13}, \mu_{23}, G_{12}, G_{13}, G_{23}\}$; Reference yielding stress $\sigma^0$ ; Anisotropic parameters $\alpha_{ij}$ ; Choose a hardening function and obtain hardening modulus $\overline{H}$;

1. Form orthotropic elastic matrix according to Eq. A.3 and calculate the total elastic stress tensor
   $\sigma_{j+1} = \sigma_j + [D]^e \, \Delta\varepsilon$
2. Calculate stress component, deviatoric stress and equivalent stress $\overline{\sigma}$ according to Eq. 3
3. Plasticity verification:
   - 3.1 Evaluate the yield function
     Eq. 3 $\rightarrow f(\sigma_{ii}) = \overline{\sigma} < 0$ ?
   - 3.2 Yes $\rightarrow$ No plasticity
     $\Delta\varepsilon_0^p = 0$
   - 3.3 No $\rightarrow$ Plasticity algorithm
     - 3.3.1 Calculate $d\overline{\varepsilon}_{pl}$ according to $\overline{H}$ and flow rule
       $d\overline{\varepsilon}_{ij}^p = \frac{df}{\overline{H}} \frac{\partial f}{\partial \sigma_{ij}}$
     - 3.3.2 Obtain equivalent plastic strain $\overline{\varepsilon}_{pl}$ and storing value of $\overline{\varepsilon}_{pl}$ in State Variables 1 $\rightarrow$ STATEV(1)
       $\overline{\varepsilon}_{pl} = \overline{\varepsilon}_{pl} + d\overline{\varepsilon}_{pl}$
4. Damage verification
   - 4.1 Obtain stress components and evaluate the damage function
     Eq.21 $\rightarrow D = \left(\frac{\overline{\sigma}}{f_{t,90}}\right)^2 + \left(\frac{\overline{\tau}}{f_{v,0}}\right)^2 < 1$ ?
   - 4.2 Yes $\rightarrow$ No damage
     - 4.2.1 Form elasto-plastic stiffness matrix $[D]$ according to Eq. B.8
     - 4.2.2 Renew stress components
       $\{\sigma_{ij}\} = \{\sigma_{ij}\} + [D]\{d\varepsilon_{ij}\}$
     - 4.2.3 Renew State Variables 2 $\rightarrow$ STATEV(2)
       STATEV(2)=1
   - 4.3 No $\rightarrow$ Damage algorithm
     - 4.3.1 Zero elasto-plastic stiffness matrix
       $[D]$=0
     - 4.3.2 Renew State Variables 2 $\rightarrow$ STATEV(2)
       STATEV(2)=0
5. Next iteration